Design, Modeling and Control of a Magnetostriction-based Force Feedback System for Robot-assisted Cardiovascular Intervention Systems

Alireza Payami

A Thesis

in

The Department

of

Mechanical, Industrial and Aerospace Engineering

Presented in Partial Fulfillment of the Requirements

for the Degree of

Master of Applied Science (Mechanical Engineering) at

Concordia University

Montréal, Québec, Canada

December

CONCORDIA UNIVERSITY

School of Graduate Studies

This is to certify that the thesis prepared

By: **Alireza Payami**

Entitled: **Design, Modeling and Control of a Magnetostriction-based Force Feedback System for Robot-assisted Cardiovascular Intervention Systems**

and submitted in partial fulfillment of the requirements for the degree of

Master of Applied Science (Mechanical Engineering)

complies with the regulations of this University and meets the accepted standards with respect to originality and quality.

Signed by the Final Examining Committee:

_____ Chair
Dr. Sivakumar Narayanswamy

_____ External Examiner
Dr. Amin Hammad

_____ Examiner
Dr. Sivakumar Narayanswamy

_____ Supervisor
Dr. Javad Dargahi

Approved by _____
Dr. Martin D. Pugh, Chair
Department of Mechanical, Industrial and Aerospace Engineering

_____ 2021

_____
Dr. Mourad Debbabi, Dean
Faculty of Engineering and Computer Science

Abstract

Design, Modeling and Control of a Magnetostriction-based Force Feedback System for Robot-assisted Cardiovascular Intervention Systems

Alireza Payami

Magnetorheological elastomers (MREs), as a class of smart materials, have a property called Magnetostriction means mechanical properties, including deformation of MREs, could be changed in response to an external magnetic field. Because of the controllable deformation, MRE is a suitable candidate for rendering the loss of haptic feedback in Robot-Assisted Cardiovascular (RCI) applications. In the recently-designed such force feedback systems, i.e. TorMag, the effect of matrix shear modulus and filler volume percentage was not studied comprehensively. Tormag also exposed limitations in force range. In the current study, a previously proposed and validated constitutive model of MREs was adopted. Then, twelve MREs with three silicon rubber matrices and four filler volume fractions were fabricated and characterized to improve the limitations mentioned above in Tormag. The average relative error between analytical force range and experiment was 10.2%, while the maximum force range was 5.29 N (stiffest matrix and 40% filler), and the minimum range was 1.06 N (softest matrix and 10% filler). Increasing filler percentage from 10% to 40% increased the force feedback range up to 288%. The state-space analysis of Tormag revealed that this system did not fully cover the required force range and zero force rendering. As an approach, structural optimization of the system is performed using the local and global optimization process. Next, a neural network (NN)-based model as the control framework was proposed and validated to obtain the necessary force for the desired input data. Then, a nearest neighbour search (NNS) method was added to the NN model to find the required magnetic field for a force-displacement profile as input. The proposed neural network accurately predicted the force-displacement behaviour of three types of MREs ($R^2 = 0.97$, mean-absolute-error=1.26 N). Also, the NN+ NNS model successfully obtained the required magnetic field (mean-absolute error=3.64 mT).

Acknowledgments

I would like to acknowledge that this master's research was performed at Concordia University during my MASc study.

First of all, I would like to dedicate my work to my Beloved wife Farzaneh and my Dear parents, Farzaneh and Mojtaba, for their love, support, inspiration, companionship, and sacrifices none of my life's achievements would have been possible.

I would like to express my gratitude to my supervisor, Prof. Javad Dargahi, for his constant support, strategic vision and giving me the opportunity of learning from him in the research were strong driving forces forward. I would like to extend my thanks to the members of the Examination Committee, Dr. Sivakumar Narayanswamy and Dr. Amin Hammador, for their time, diligent advice, and guidance throughout my study. My special thanks and gratitude go to my mentor, Dr. Amir Hooshiar, whose technical knowledge, professionalism, and modesty made him a role model for my future career. I want to extend my thanks to Dr. Ahmedreza Arshi and Dr. Hamidreza Katouzian from Amirkabir University of Technology, who have constantly supported me since my previous graduate study in Iran.

I appreciate the financial support of Natural Sciences and Engineering Research Council of Canada for granting me an NSERC CREATE Masters Fellowship for Surgical Innovation. Moreover, I would like to thank the staff of the Mechanical, Industrial, and Aerospace Engineering Department for their kind support.

Contents

List of Figures

List of Tables

Nomenclature

Symbols

Operators

$\otimes$	Outer product

Greek Symbols

$\lambda_{1,2,3}$	Principal stretches
$\mathbf{\Lambda}$	Left Cauchy-Green deformation tensor
μ_0	Magnetic permeability of vacuum
μ_r	Relative magnetic permeability
ρ	Density
σ_i	Normal true stress at inner radius
Ω	strain energy
$\Omega^\star$	Total amended free energy function
ξ	Traction coefficient
ζ	Volume fraction of CIP in MRE

English Symbols

$\mathbf{b}$	Magnetic field intensity
b_R	Radial component of the magnetic field intensity
b_Z	Longitudinal component of the magnetic field intensity
$\mathbf{C}$	Right Cauchy-Green deformation tensor
D_r	Diameter of the active roller

$\hat{\mathbf{e}}_{(.)}$	Unit vector in $(.)-$direction
e_{ss}	Steady-state error
E	Elastic modulus
$\mathbf{f}_f$	Friction force vector
$\mathbf{F}$	Deformation gradient tensor
$F^\star$	Desired force
F_{ATI}	Reference force measured by ATI Mini40 sensor
F_{max}	Maximum force
G_0	Initial shear modulus
$\mathbf{h}$	Magnetic field strength
H	Transfer function of DC-motor in $z-$space
$\mathbf{I}$	3-by-3 identity matrix
$I_{1\cdots6}$	Scalar magnetoelastic deformation invariants
$k_{P,I,D}$	Coefficients of PID controller
N_p	Number of peak forces
p	Lagrange multiplier
r	Radial distance in radial coordinate system
R_i	Inner radius
R_o	Outer radius
R^2	Goodness-of-fit
s	magnet separation
t	Time, thickness
$\mathbf{t}$	Position vector of the tip of catheter
T	Torque
$\mathbf{T}$	Nominal stress tensor
$T_{5\%}$	Settling time (5%-variation)
T_r	Resistant torque, Rise time
T_f	Frictional torque

$\mathbf{x}$	Spatial representation of the coordinates
$\mathbf{X}$	Material representation of the coordinates
y	y-component of the tip position of catheter
z	Longitudinal distance in cylindrical coordinate system

Abbreviations

AFib	Atrial fibrillation
ANN	Artificial neural network
DC	Direct current
EV	Endovascular
FEM	Finite-element method
FFNN	Feed-forward neural network
GUI	Graphical user interface
ID	Inner diameter
LHS	Left-hand-side
MAE	Mean-absolute error
MIS	Minimally invasive surgery
MRE	Magnetorheological elastomer
MRF	Magnetorheological fluid
NL-FEM	Nonlinear finite-element method
NN	Neural network
kNN	k-nearest neighbor method
OD	Outer diameter
PCI	Percutaneous cardiovascular intervention
PID	Proportional integral derivative
RCI	Robot-assisted cardiovascular intervention
RFA	Radio-frequency ablation
RMS	Root-mean-square
SD	Standard deviation
SMA	Shape memory alloy

Chapter 1

Introduction

1.1 Background

Cardiovascular diseases (CVDs) are the first cause of mortality, hospitalization, and medical prescriptions around the world, and forecasts show the continuation of this trend in the foreseeable future [1]. Among CVDs, Coronary Artery Stenosis (CAS) is the most prevalent [2]. This disorder occurs when major blood vessels are blocked with the build of one or multiple lipids or calcified plaques. CAS compromises the blood flow to myocardial tissue and can lead to myocardial infarction, stroke and even death. CAS is shown in Fig.1.1. The blockage could be categorized into three levels; low, medium and high. For low-level blockage (lower than 30%), the proper treatment is medication. This method is suitable for low drug-resistant patients and low age, but low efficiency is a limitation. Proper treatment for medium blockages (31$\sim$50%) is catheter intervention. This minimally invasive method is the correct answer for no drug-affected patients, but access to vessels is limited and indirect. In high blockages (more than 50%), the needful treatment is open-heart surgery. This method leads to complete cure, but high hemorrhage and the high mortality rate is a limitation.

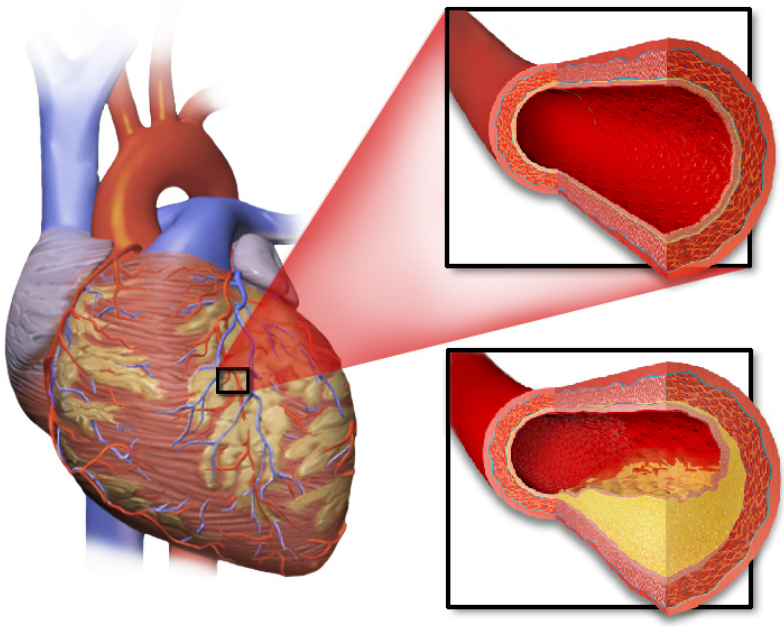

Figure 1.1: Schematic view of a representative coronary artery stenosis.

1.1.1 Percutaneous Intervention

Minimally invasive cardiac intervention, a.k.a. percutaneous intervention, is the gold standard treatment for the majority of cardiovascular diseases, e.g., vascular stenosis and arrhythmia [3, 4]. Because of its percutaneous approach, interventional surgery is performed under live x-ray imaging, i.e., fluoroscopy. Continuous x-ray exposure has been shown to expose surgeons and patients to chronic health risks, such as radiation-related orthopedic diseases, cataracts and skin cancer[5–7]. Other risks are ionizing radiation and glove perforation for surgeons and over injection of contrast agents for patients[6, 7].

1.1.2 Robot-assisted Cardiovascular Intervention

Robot-assisted cardiovascular interventional (RCI) systems have been used in clinics to improve functionality and alleviate the limitations of percutaneous intervention, e.g. X-ray exposure. They were commercialized in 2012, and some models are CorePath200 (2012), Magellan (2013) and

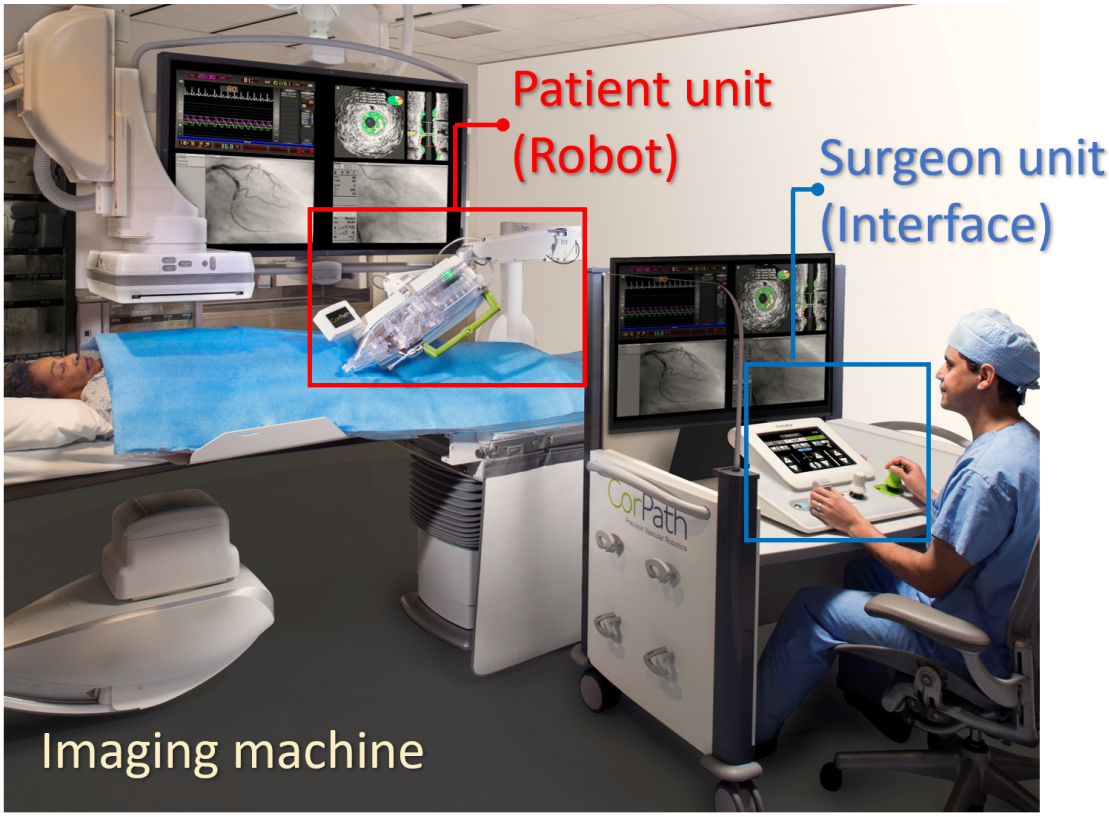

Figure 1.2: Components of a representative RCI system with master-slave configuration (Courtesy of Corindus Inc., Waltham, MA, USA).

CorePathGRX (2016). These systems could be exploited in various disciplines, including cardiology and orthopedic surgeries, laparoscopy, neurosurgery, and emergency response [8]. RCI systems utilize master–slave robotic configurations and put the surgeon at a safe distance from the x-ray imaging machine [9, 10]. Fig. 1.2 shows a representative master–slave RCI system. Despite RCI's advantage in reducing the exposure-related health risks, studies have indicated the loss of haptic feedback as to its prime limitation. The loss of haptic feedback may lead to poor hand–eye coordination and compromised perception of vascular anatomy [9]. Also, RCI systems have improved the geometric precision in stent placement and increased the dexterity in interventional tasks [11, 12]. Moreover, RCI systems have enabled surgeons to perform long-distance tele-intervention safely and effectively [13].

1.1.3 Limitations of the State-of-the-art

The loss of haptic feedback has been reported as the main limitation of the state-of-the-art [9]. There are multiple reasons indicated in the literature for this limitation. Serious concerns about the loss of haptic feedback during robotic interventions are expressed in clinical investigations [10, 11, 14, 15]. Seto et al. [16], and Smilowitz et al. [17] have likened the robotic intervention without haptic feedback to a blind control of catheter and guidewire. The first difficulty inherited by the loss of haptic feedback in robotic intervention is the poor hand-eye coordination [18]. Consequently, a surgeon's geometric perception of the catheter and vessels gets limited [11], [12, 19–21]. It is also postulated to contribute to guidewire oversteering and vascular rupture [22]. Furthermore, studies have shown that significant risk of embolization, perforation, thrombosis, and dissection is associated with excessive contact force between the catheter and vascular wall [12, 19, 20], [22], [23]. Uncertainty about the catheter insertion force and depth are reported as causes of withdrawal of the robotic procedures [5], [16], [24], [11]. Rafii-Tari et al. [20] have recently identified significantly different force-time signatures between novice and expert interventionists in five common robotic interventional procedures. Also, it is observed that the pulling force for the novices group was up to six times larger than experts. On the other hand, other studies have reported up to 76% reduction in the contact force between catheter and vessel by providing force feedback to a surgeon in a simulated aortic cannulation [12], [25]. Also, studies have revealed that the effectiveness of robotic EPI procedures are significantly dependent on the ability of the surgeon to maintain the contact force in the range of 20$\pm$ 10 grf [26],[27]. Furthermore, a recent study has shown that the motor reaction of the catheter is faster than the visual reaction time. This postulates the possibility of early risk prevention with haptic feedback [28]. Therefore, the role of haptic feedback in the safety and effectiveness of robotic interventions is evident.

1.2 Problem Definition

The main limitation of RCI is the loss of haptic feedback. Loss of haptic feedback reduces the situational awareness of the surgeon and increases the risk of vascular rupture due to over-steering of the surgical instruments [11, 18, 19]. Also, in the absence of haptic feedback, control on catheter

and guidewire reduces noticeably. Without haptic feedback, applied force to the catheter and depth of insertion could not be estimated precisely [29].

1.3 Research Objectives

In recently-designed force feedback systems in RCI applications, i.e. TorMag, there was a limitation for force range rendering and insufficient studies on the effect of matrix shear modulus and filler volume percentage on the force range. On the other hand, the phase portrait analysis has shown that the TorMag system was not structurally-optimized for full coverage of force range and zero force rendering. Moreover, instead of the current PID controller used in the control framework of TorMag, there was feasibility to apply a neural network-based controller. This research aims to propose and validate a haptic force feedback system based on composite magneto-rheological elastomers for robot-assisted cardiovascular intervention applications. To this end, the following aims were considered:

(1) A comprehensive study on the effect of shear modulus matrix and filler of MREs in the force range of recently-developed force feedback system (TorMag) and finding suitable MRE type for various surgeries,

(2) Structural optimization of TorMag and alleviating its performance by utilization of Phase Portrait concept and definition of the suitable goal function,

(3) Introducing a feasible Artificial Neural Network (ANN)-based controller for torque feedback applications.

1.4 Literature Review

1.4.1 Force rendering modalities

For haptic rendering, researchers have adopted three approaches: active, passive, and semi-active approach. Each of them has different sub-approaches. Active modality includes DC-motor and SMA (Shape Memory Alloys). For Passive modality, the sub-categories are constant friction and

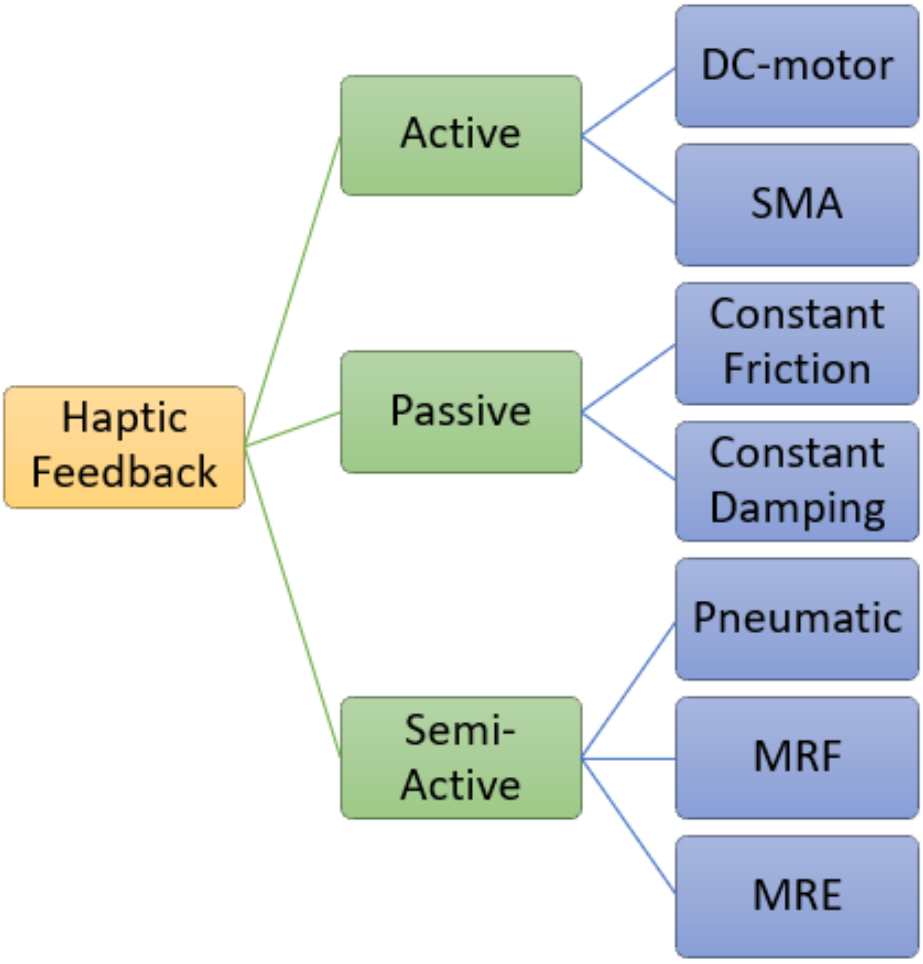

Figure 1.3: Modalities for rendering haptic feedback.

constant damping. The Pneumatic, MRF (Magnetorheological Fluids) and MRE (Magneto-rheological Elastomers) methods could be mentioned in semi-active modality. These modalities are shown in Fig. 1.3.

Each of these modalities has its cons and pros, but power consumption, controllability, and instability are crucial factors for comparing them. Table 1.1 compares these approaches.
Based on the literature review, it is evident that controllability in the passive method is zero, whereas semi-active materials, including MREs and MRFs, offer medium controllability. The active methods, e.g., DC motors and SMAs, are good in controllability of the force or torque, but they have limitations in power consumption and instability in high range forces. Semi-active materials have low power consumption and high stability at the extreme load capacity [9, 9, 30].

Also, researchers have proposed various sensor-based [31–33] and sensor-free [34–36, 36] methods to obtain the haptic (contact) forces at the patient side in parallel to haptic rendering at the surgeon side. In addition, haptic rendering has been recently used with cloud-connected wearable devices for seamless integration with existing RCI systems [37].

Recent studies have proposed various methods for force feedback rendering for telerobotic intervention applications. In the following representation, such as use of magnetorheological fluids (MRF) [38–40], electroactive polymers (EAP) [41], shape-memory alloys (SMA) [42], direct-drive electric motors [34], and magnetorheological elastomers (MRE) [30, 43]. MREs are a class of smart composites composed of a polymeric matrix, e.g., silicon rubber, a ferromagnetic filler, e.g., carbonyl iron particles (CIP), and additives, e.g., silicon thinner and slacker. Upon exposure to the external magnetic field, the ferromagnetic filler particles conform their magnetic dipole to the field, thus causing local strain within the MRE [44]. Given that the matrix of MRE is hyperelastic with strain-stiffening [45, 46], and since the magnetic-induced deformation increases the strain within the MRE, its stiffness increases.

From a practical point of view, the performance of the proposed methods in the literature differs in simplicity, passive stiffness, force range, and size. More specifically, Table 1.1 compares a set of representative studies in the literature. For force feedback rendering, Mazursky *et al.* [40] proposed a slim haptic actuator conveying both kinesthetic and vibrotactile information to the user. Being electrically active and feed-forward is limiting the applicability of their work.

Han *et al.* [41] proposed an MR-compatible haptic display that functioned by eliciting skin stretch in the proximal/distal direction when a user held it between the thumb and index finger. The device was intended to display forces sensed at the tip of a tool, such as an instrumented biopsy needle, during MR-guided interventions. This system was inherently directional, and later works could display static as well as dynamic forces.

Kanjanapas *et al.* [47] generated compressive forces using two degrees of freedom (DoF) pneumatic soft linear tactor mounted on the subject's forearm. While it could generate haptic cues with a favourable resolution, its manufacturability was cumbersome due to its complex design.

Culjat *et al.* [48] developed a pneumatic balloon-based system to provide tactile feedback to the fingers of the surgeon during robotic surgery. Similar to [47], zero passive stiffness has increased

Table 1.1: Comparison of representative studies proposing haptic rendering for the minimally invasive surgery applications.

Study	Principle	Advantages	Limitations
Oh *et al.* [38] (2013)	MRF*	Passive stiffness simplicity force range	Electrically active not MRI-safe
Han *et al.* [41] (2018)	EAP†	MRI-safe passive stiffness	Complexity electrically active
Yanatori *et al.* [42] (2019)	SMA‡	Passive stiffness simple	Electrically active not MRI-safe, range
Mazursky *et al.* [40] (2019)	MRF	Passive stiffness simplicity range low profile	Electrically active not MRI-safe
Hooshiar *et al.* [30] (2020)	MRE	Passive stiffness simplicity range low profile electrically passive	not MRI-safe
Hooshiar *et al.* [43] (2021)	MRE	Passive stiffness simplicity size electrically passive	not MRI-safe force range

*MRF: Magneto-rheological fluid
†EAP: electro-active polymer
‡SMA: shape-memory alloy

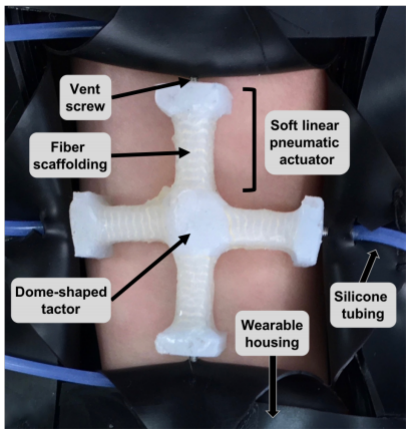

Figure 1.4: A 2-DoF soft haptic device comprised of four fiber-constrained linear pneumatic actuators connected to a dome-shaped tactor head, and attached to a wearable housing by Kanjanapas *et al.* [47].

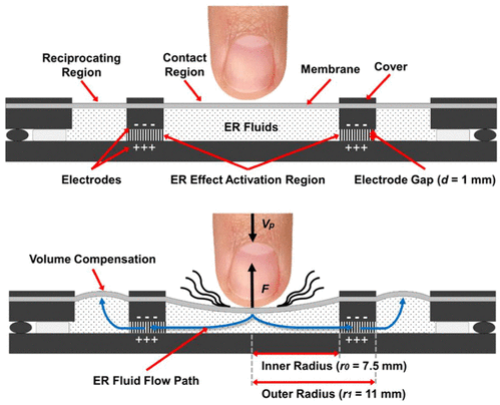

Figure 1.5: Working principle of an MRF-based haptic actuator (a) before contact and (b) mid-contact by Mazursky *et al.* [40].

the lower limit of the bandwidth of their system. However, using a pneumatic system has significantly limited their proposed solution for torque feedback applications due to the low upper limit of the bandwidth.

Magnetorheological fluids (MRFs) have also been used as feedback media, e.g., [49–51]. However, handling MRFs (due to their fluidic state) and accumulation of heat, which drastically changes the mechanical properties of MRFs, have been reported as their prime limitations [30].

In 2020, utilization of MRE as a tactile medium was proposed by Hooshiar *et al.* [30]. To control the stiffness and force of an enhanced composite MRE, they controlled the distance between a pair of permanent N52 magnets that generated the magnetic field on the MRE. Their MRE-based system exhibited acceptable compliance with the functional and physical requirements of haptic displays for robot-assisted surgery.

In 2021, Hooshiar *et al.* [43] proposed a force feedback modality based on frictional torque generation between a ferromagnetic shaft and a hollow cylindrical MRE for RCI applications. Their study showed the feasibility of force feedback through the magnetostriction phenomenon; however, it was limited to using only one MRE type, i.e., EcoFlex 00-50 with 40% CIP.

1.4.2 Force feedback requirements

Previous studies show that for robot-assisted cardiovascular interventional surgery, a haptic force (F) of 0-2 N is required [9], with a resolution of 5% of full-scale equals that is 0.1 N. The output

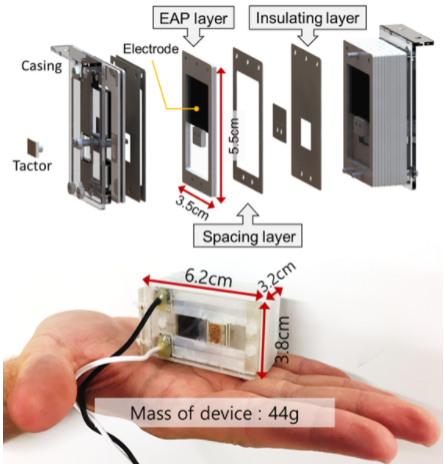

Figure 1.6: Exploded view of an EAP-based haptic device by Han *et al.* [41].

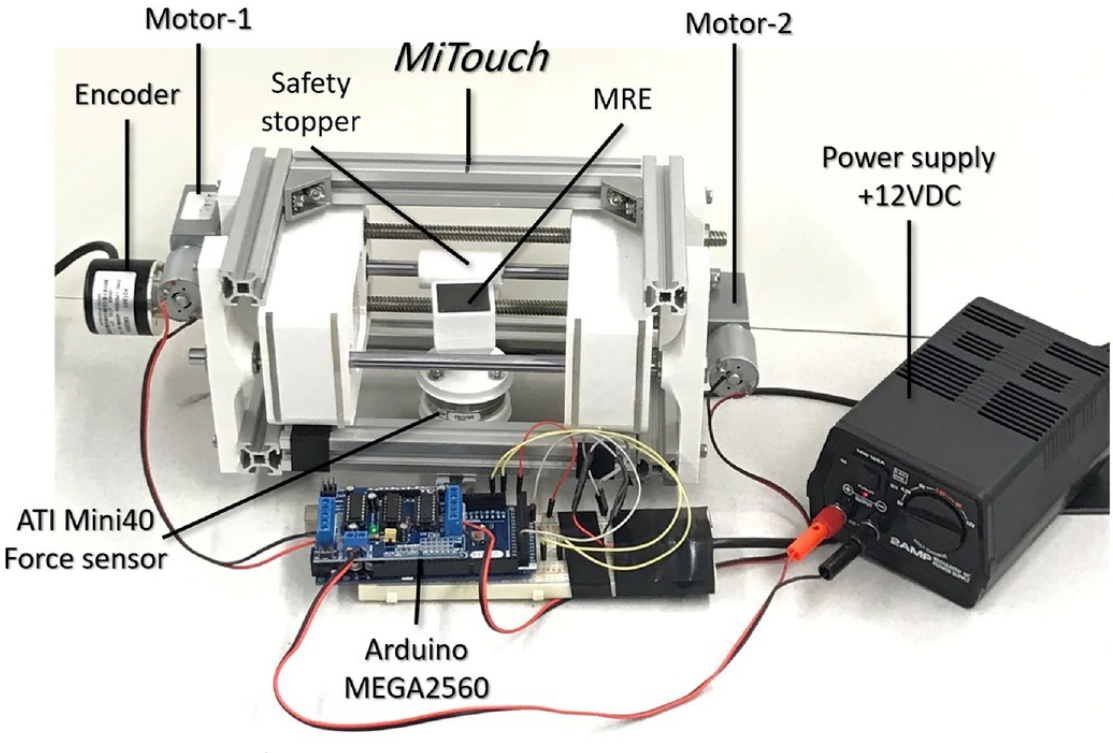

Figure 1.7: An MRE-based tactile display by Hooshiar *et al.* [30].

shaft of TorMag is coupled to a roller with a radius of 20 mm. Therefore, the required torque range to generate a linear force of 0-2N is 0–40 mNm with a resolution of 2 mNm.

1.5 Contributions

The author has made the following contributions during this research:

(1) Alireza Payami, Javad Dargahi, and Amir Hooshiar. Performance analysis of magnetorheological elastomer composites for telerobotic force feedback rendering. *Advanced Composites and Hybrid Materials (under-review)*, 2021,

(2) Amir Hooshiar, Alireza Payami, Javad Dargahi, and Siamak Najarian. Magnetostriction-based force feedback for robot-assisted cardiovascular surgery using smart magnetorheological elastomers. *Mechanical Systems and Signal Processing*, 161:107918, 2021,

(3) Alireza Payami, Javad Dargahi, and Amir Hooshiar. Structural optimization of a magnetostriction-based force feedback system for telerobotic intervention. In *2021 IEEE International Symposium on Robotic and Sensors Environments (ROSE) (ROSE 2021)*, pages 1–7. IEEE, 2021,

(4) Alireza Payami, Amir Hooshiar, Ali Alkhalaf, and Javad Dargahi. Modeling of rate-dependent force-displacement behavior of mres using neural networks for torque feedback applications. In *2020 8th International Conference on Control, Mechatronics and Automation (ICCMA)*, pages 58–62. IEEE, 2020.

1.6 Dissertation Layout

This thesis is structured in a manuscript form and consists of the following five chapters and two appendices:

Chapter 1 provides the introduction for the studied topic as well as background, problem definition, objectives, literature review, and contributions.

Chapter 2 summarizes the modeling and investigation of the effects of properties of the MREs on the force range of the haptic device.

Chapter 3 presents an optimization study to enhance the performance of the proposed haptic device through geometry optimization of the MRE and the haptic device.

Chapter 4 a neural network model was proposed and validated for the rate-dependent force-displacement behaviour of MREs. This NN model was trained by previously available experimental data (including displacement, displacement rate, magnetic field intensity and Carbonyl Iron Particle (CIP) percentage of MRE) as input to predict the required magnetic field for a given force.

Chapter 5 presents the conclusions and future works of this research. Also, the research limitations are acknowledged, and mitigation measures are proposed for future works.

Appendix A presents the Matlab code developed to estimate the phase-portrait of the haptic device.

Appendix B presents the optimization code for obtaining structurally-optimized design of the haptic device.

Chapter 2

Performance Analysis of Magnetorheological Elastomer Composites for Telerobotic Force Feedback Rendering

The magnetostriction phenomenon of magnetorheological elastomer (MRE) composites have been recently used for rendering force feedback for remote surgical applications. Despite the exhibited feasibility, the proposed designs have shown limitation in force range and zero-force rendering. In addition, present literature lack a comprehensive study on the effect of matrix shear modulus and filler volume percentage on the force range of such force feedback systems. Therefore, in this study, first a previously proposed and validated constitutive model of MREs was adopted and improved to accommodate the effect of changing the filler volume fraction. Afterward, twelve MREs with three silicon rubber matrices, and four filler volume fractions, were fabricated and characterized for shear modulus and force feedback range. The results showed fair agreement between the proposed constitutive model and experimental observation. The average relative error between analytical force range and experiment was 10.2%, while the maximum force range was 5.29 N (stiffest matrix and 40% filler) and the minimum range was 1.06 N (softest matrix and 10% filler). Also, both filler

volume fraction and shear modulus of the matrix had positive correlation with the force feedback range. Increasing filler percentage from 10% to 40% increased the force feedback range up to 288%. However, minimum force feedback increases with the filler volume fraction that might be related to magnetization and residual magnetostriction at low magnetic fields. In the end, by comparison with the requirements of various remote surgical procedures, it was shown that one or multiple MREs could be used for each specific surgical procedure.

2.1 Study Objectives

The objective of this study was to investigate the performance of various CIP-percentage and matrix mechanical properties on the force range of the proposed system. Therefore, a previously validated constitutive model for the MREs used in this force rendering modality, simulated the effect of changes in the matrix mechanical properties and CIP percentage, and experimentally characterized the effect of changes in them on the force rendering capacity of the proposed force feedback system.

2.2 Related Studies

Recent studies have proposed various methods for force feedback rendering for telerobotic intervention applications. In the following representati, such as use of magnetorheological fluids (MRF) [38–40], electroactive polymers (EAP) [41], shape-memory alloys (SMA) [42], direct-drive electric motors [34], and magnetorheological elastomers (MRE) [30, 43]. MREs are a class of smart composites composed of a polymeric matrix, e.g., silicon rubber, a ferromagnetic filler, e.g., carbonyl iron particles (CIP), and additives, e.g., silicon thinner and slacker. Upon exposure to external magnetic field, the ferromagnetic filler particles conform their magnetic dipole to the field thus cause local strain within the MRE [44]. Given that the matrix of MRE is hyperelastic with strain-stiffening [45, 46], and since the magnetic-induced deformation increases the strain within the MRE, its stiffness increases.

From a practical point of view, the performance of the proposed methods in the literature differ in simplicity, passive stiffness, force range, and size. More specifically, Table 2.1 compares a set of representative studies in the literature.

Table 2.1: Comparison of representative studies proposing haptic rendering for the minimally invasive surgery applicatiosns.

Study	Principle	Advantages	Limitations
Oh *et al.* [38] (2013)	MRF*	Passive stiffness simplicity force range	Electrically active not MRI-safe
Han *et al.* [41] (2018)	EAP†	MRI-safe passive stiffness	Complexity electrically active
Yanatori *et al.* [42] (2019)	SMA‡	Passive stiffness simple	Electrically active not MRI-safe, range
Mazursky *et al.* [40] (2019)	MRF	Passive stiffness simplicity range low profile	Electrically active not MRI-safe
Hooshiar *et al.* [30] (2020)	MRE	Passive stiffness simplicity range low profile electrically passive	not MRI-safe
Hooshiar *et al.* [43] (2021)	MRE	Passive stiffness simplicity size electrically passive	not MRI-safe force range

*MRF: Magneto-rheological fluid
†EAP: electro-active polymer
‡SMA: shape-memory alloy

For force feedback rendering, Kanjanapas *et al.* [47] generated compressive forces using a two degrees of freedom (DoF) pneumatic soft linear tactor mounted on the subject's forearm. While it could generate haptic cues with favorable resolution, its manufacturability was cumbersome due to complex design. Mazursky *et al.* [40] proposed a slim haptic actuator that generated both kinesthic and vibrotactile feedbacks, however their system was electrically active that principally has safety concerns.

In 2020, utilization of MRE as tactile medium was proposed in [30]. To control the stiffness and force of an enhanced composite MRE, they controlled the distance between a pair of permanent N52 magnets that generated the magnetic field on the MRE. Their MRE-based system exhibited acceptable compliance with the functional and physical requirements of haptic displays for robot-assisted surgery. In continuation, a force feedback modality based on frictional torque generation between a ferromagnetic shaft and a hollow cylindrical MRE was co-developed by the author for RCI applications. Their study showed the feasibility of force feedback through magnetostriction phenomenon, however, it was limited to using only one MRE type, i.e., EcoFlex 00-50 with 40% CIP. In addition, Payami *et al.* [46] proposed a neural network based method for controlling frictional torque of MRE on the output shaft of their device. In their study, they successfully generated blood pressure pulse forces in a telerobotic RCI system.

Based on the literature, MREs are the most recent class of materials proposed for semi-active haptic rendering [43]. Also, MREs exhibit versatile applications such as rapid prototyping [54], self healing [55], and sensing capability [56].

It has been shown that MREs are a well-suited class of materials to be used for haptic and tactile rendering due to their intrinsic compatibility with the physical and functional requirements of such systems for RCI tasks [30, 43]. They also have shown the feasibility of using this phenomenon as a stiffness feedback [30, 57, 58] and force feedback [43, 46] rendering methods. However, the effects the mechanical properties of the matrix polymer and percentage of CIP on the performance of the previously proposed MRE-based force rendering method has not been studied. Recent studies have shown prominent effect of filler composition and magnetic properties on the magnetorheological properties of the MREs, e.g., [54, 59]. Thus, it was hypothesized that it might be possible to tune and adapt the force feedback range of MREs for different applications through changing the filler

volume fraction and shear modulus of the matrix.

In the following, the force feedback system design, MRE fabrication, magnetic field generation, and magnetoelastic modeling are provided in Sec. 2.3. Afterwards, the protocol, results, and discussion of the validation study are provided in Sec. 2.4 and are followed by the key findings, concluding remarks, and future works in Sec. 2.5.

2.3 Material and Methods

2.3.1 System design

The author has previously shown the feasibility of a magnetostriction-based force feedback system, i.e., TorMag in [43]. Fig. 2.1(a–d) depicts the conceptual magnetic field distribution between two permanent magnets, the MRE and system components, prototyped device, and integrated prototype with a representative surgeon interface of an RCI system. In summary, the magnetic field would cause magnetostriction, i.e., compressive force on the output shaft and friction thereof, which was transmitted to the hand of surgeon utilizing a double roller design Fig. 2.1(d) [43]. This device was used in this study to perform the validation tests. The geometrical dimensions of the MRE and force feedback device in this study are provided in Table 2.2.

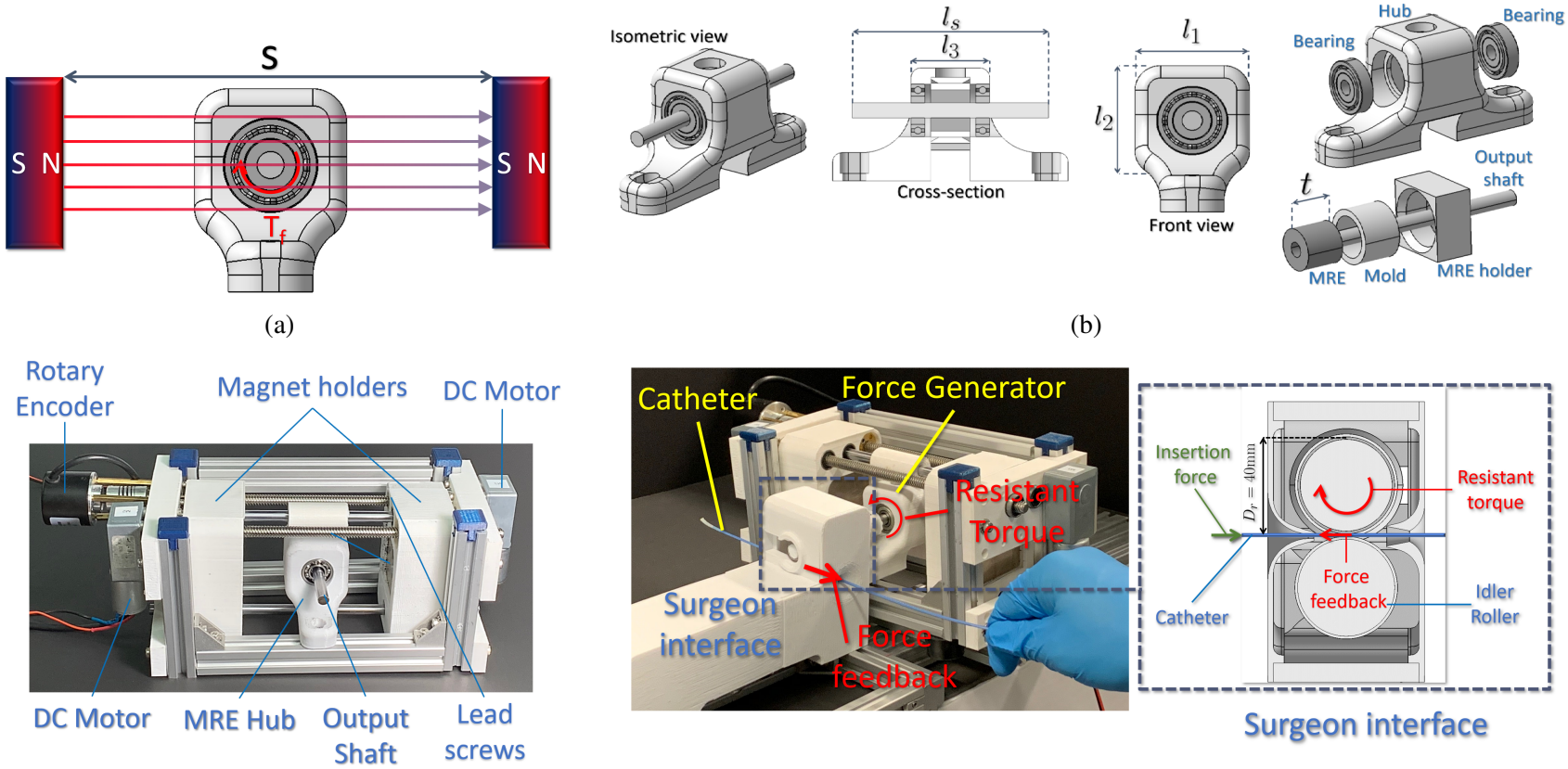

Figure 2.1: (a) Schematic placement of TorMag in external magnetic field, (b) components of the force feedback system, (c) prototyped system, and (d) integration of the force feedback system with a representative surgeon interface for RCI application.

Table 2.2: Geometrical dimensions of TorMag for RCI application.

	MRE Cylinder			Shaft	Housing		
Dimension	R_o	R_i	t	l_s	l_1	l_2	l_3
(mm)	11	4	20	75	40	45	40

The presented design would result in a fairly radial magnetic field inside the MRE [43]. Due to the circumferential symmetry, a homogeneous radial contact stress is present at the interface of the output shaft and the MRE [43]. The system also used two rare earth permanent magnets N52 to generate the external magnetic field. This configuration is previously used in [57] for generating steady-state magnetic field in the absence of a ferromagnetic shaft.

2.3.2 MRE fabrication

MRE samples used in this study were isotropic and were composed of silicon rubber matrix (Ecoflex™, Smooth-On Inc., PA, USA), CIP filler (SQ, BASF, Germany), Slacker (Smooth-On Inc., PA, USA) and silicon thinner (Smooth-On Inc., PA, USA). The CIP had a nominal mean particle diameter of 45μm with less than 5% variation. Also, silicon oil (Slacker™) and silicon thinner were used as additives in the emulsions to enhance their moldability.

To investigate the effect of matrix's mechanical properties, their initial shear moduli, $G_\circ$ were selected as the indicator [57]. For the CIPs, the volume fraction was considered as the indicator. In total twelve different MREs were fabricated with different matrices and filler percentages. For each MRE, three identical samples were fabricated and used in the study.

For MRE fabrication, direct molding was used. The molds were prototyped with poly-lactic acid (PLA) filaments using a 3D-printer (Replicator+, Makerbot Industries LLC, NY, USA). The mold components were assembled as shown in Fig. 2.2(a). After mixture, the MRE emulsions were degassed inside a vacuum chamber at -29 inHg gage pressure. Next the emulsions were poured into the molds and were rested for 24 hours at standard laboratory conditions. In the end, the MRE molds were assembled on the MRE hub and inserted into the device. Fig. 2.2(a) schematically depicts the MRE mold assembly and positioning inside the device and Fig. 2.2(b) depicts the twelve MRE samples moulded.

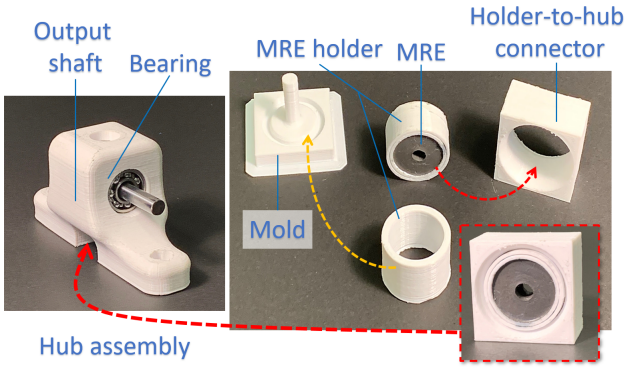

(a)

(b)

Figure 2.2: (a) Mold structure and assembly of MREs into the force feedback device, (b) molded MREs used in this study.

Previous studies, e.g., [44, 60] have reported enhanced properties with MRES composed of up to 40% volume fraction of CIP. Also, silicon rubbers with shore hardness of 00-10, 00-30-, and 00-50 have been used to exhibit favorable magnetostriction effects. Therefore, in this study, three matrix polymer with different shore hardnesses, i.e., 00-10, 00-30, and 00-50, were used. Also, each matrix was filled with four different CIP percentage, i.e., 10%, 20%, 30%, and 40% volume fraction. The MREs reported in this study were labeled according to their matrix and filler percentage. The MRE labels and volume fraction of their components are summarized in Table 2.3.

Table 2.3: Density, mass, and volume percentage of the contents of the fabricated MREs.

Material	Shore hardness (matrix)	Contents (per 100 cc) (%vol., mass)				Shear Modulus $G_\circ$ (kPa)
		Matrix (Ecoflex) $\rho_M = 1.04\frac{g}{cc}$	Filler (CIP) $\rho_F = 7.87\frac{g}{cc}$	Additive (Slacker) $\rho_S = 0.97\frac{g}{cc}$	Additive (Thinner) $\rho_T = 0.97\frac{g}{cc}$	
MRE-10-10	10	80%, 83.2g	10%, 78.7g	5%, 4.9g	5%, 4.9g	79.5
MRE-10-20	10	70%, 72.8g	20%, 157.4g	5%, 4.9g	5%, 4.9g	106.4
MRE-10-30	10	60%, 62.4g	30%, 236.1g	5%, 4.9g	5%, 4.9g	139.9
MRE-10-40	10	50%, 52.0g	40%, 314.8g	5%, 4.9g	5%, 4.9g	175.0
MRE-30-10	30	80%, 83.2g	10%, 78.7g	5%, 4.9g	5%, 4.9g	87.2
MRE-30-20	30	70%, 72.8g	20%, 157.4g	5%, 4.9g	5%, 4.9g	120.1
MRE-30-30	30	60%, 62.4g	30%, 236.1g	5%, 4.9g	5%, 4.9g	144.8
MRE-30-40	30	50%, 52.0g	40%, 314.8g	5%, 4.9g	5%, 4.9g	188.5
MRE-50-10	50	80%, 83.2g	10%, 78.7g	5%, 4.9g	5%, 4.9g	88.9
MRE-50-20	50	70%, 72.8g	20%, 157.4g	5%, 4.9g	5%, 4.9g	137.6
MRE-50-30	50	60%, 62.4g	30%, 236.1g	5%, 4.9g	5%, 4.9g	185.5
MRE-50-40	50	50%, 52.0g	40%, 314.8g	5%, 4.9g	5%, 4.9g	277.3

2.3.3 Shear Modulus Characterization

In order to characterize the initial shear moduli of the prepared MREs, three cylindrical samples of each MRE were prepared and tested in compression according to the standard test method in ISO 7743 [61]. The samples were of cylindrical shape with a diameter of $D_\circ = 30$mm and a height of $H_\circ = 12.5$mm. The cyclic uniaxial compression test was repeated three times for each MRE. In each test, initially the sample underwent three conditioning cycles up to 25% strain and the data of the fourth cycle was used in shear modulus calculation. The engineering stress σ and stretch λ of the samples were calculated using [61]:

$$\sigma = \frac{\hat{F}}{A_\circ}, \tag{1}$$

$$\lambda = 1 + \frac{\delta}{H_\circ}, \tag{2}$$

where, $\hat{F}$ was compressive force, $A_\circ = \pi\frac{D_\circ^2}{4}\text{mm}^2$ was the undeformed cross-sectional area of the samples, δ was the compressive deformation, and $H_\circ = 12.5$mm was the undeformed height of the samples. To calculate the shear moduli of the samples, the stress–stretch curves were fitted with

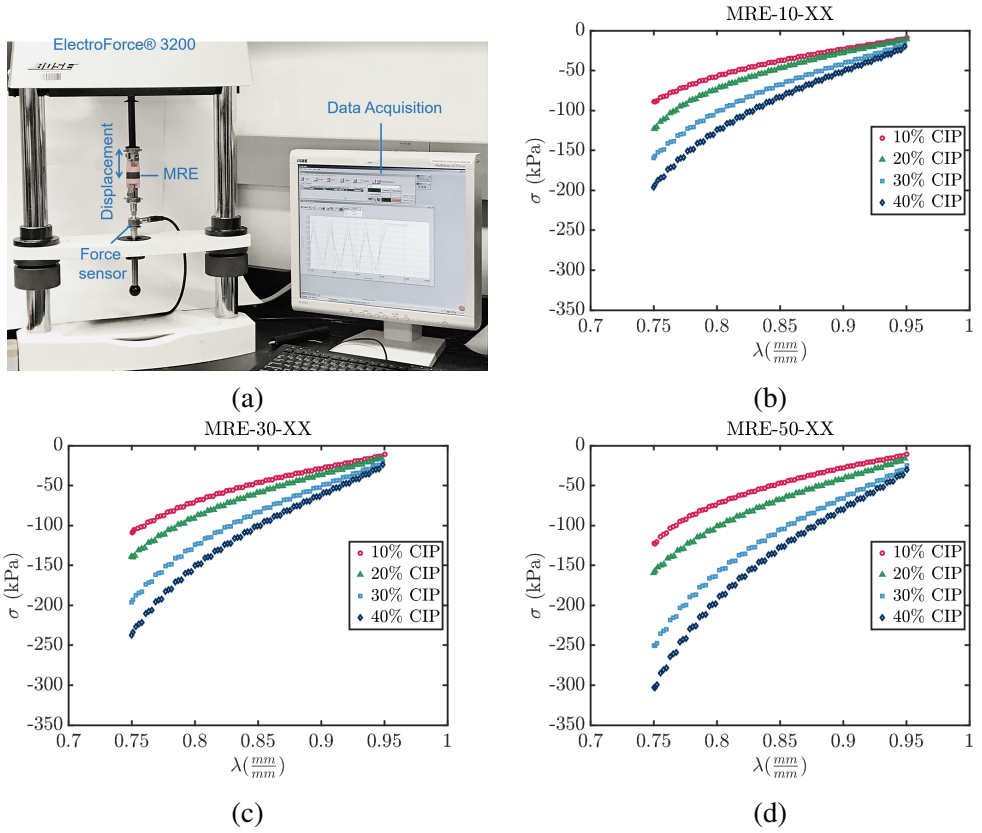

Figure 2.3: (a) Test setup used in shear modulus characterization, and stress–stretch diagrams of (b) MRE-10-XX, (c) MRE-30-XX, and (d) MRE-50-XX.

incompressible single-term Ogden model [57]:

$$\sigma = G_{\circ}(\lambda^{\alpha} - \lambda^{-\frac{\alpha}{2}}), \tag{3}$$

where shear modulus $G_{\circ}$ and α were the fitting parameters. The fitting was performed in Matlab R21a (Mathworks Inc., MA, USA). The average goodness-of-fit for the curve fittings was 97.65%. Fig. 2.3(a) depicts the test setup and Fig. 2.3(b–d) shows the stress–stretch diagrams of the samples. Also, the shear moduli of the MREs are reported in Table 2.3.

2.3.4 Magnetic field and permeability

For controlling the magnetic field intensity, the gap distance between the magnets (s in Fig. 2.1(a)) was controlled using two synchronized lead screws. This mechanism was shown to generate up to 800 mT magnetic field with direct Gaussmetery measurement [43, 46].

The magnetic field intensity $\mathbf{h}$ and magnetic flux density $\mathbf{b}$ are linearly related with the relative permeability coefficient μ_r such that:

$$\mathbf{b} = \mu_0 \mu_r \mathbf{h}, \tag{4}$$

with $\mu_0 = 4\pi \times 10^{-7} \frac{H}{m}$. The relative permeability of similar MREs μ_r are reported to vary linearly between $\mu_r \approx 2$ and $\mu_r \approx 4$ with CIP percentages of 10% to 40% [54, 62, 63]. Thus, the following μ_r was assumed as:

$$\mu_r(\zeta) = 2 + \frac{2(\zeta - 10\%)}{30\%}, \tag{5}$$

where, ζ was the CIP volume fraction. IT has been shown that the magnetic field within the MRE is of the form [43]:

$$\mathbf{b} = \frac{a(s)}{R}\hat{\mathbf{e}}_R. \tag{6}$$

with $\hat{\mathbf{e}}_R$ radial unit vector, and:

$$a(s) = c_1(s_{max} - s)^p + c_2, \tag{7}$$

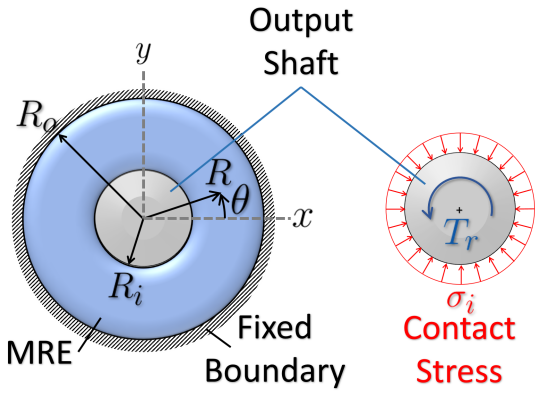

Figure 2.4: Geometry of the transverse cross-section of the shaft and MRE with fixed boundary conditions at outer radius (left) and the free-body diagram of the output shaft (right).

with $s_{max} = 95$mm, $c_1 = 1.206$, $c_2 = 1256$, and $p = 1.867$ [43]. Therefore, the magnetic field intensity within the MRE is proportional to the CIP volume fraction ζ:

$$\mathbf{h} = \mu_0^{-1}(2 + \frac{2(\zeta - 10\%)}{30\%})^{-1}\frac{c_1(s_{max} - s)^p + c_2}{R}, \tag{8}$$

where, R is the radial position inside MRE with respect to its longitudinal axis (cylindrical coordinates).

2.3.5 Magnetoelastic modeling

2.3.6 Geometry and domain

Fig. 2.4 shows the schematic geometries of the MRE and the free-body diagram of the output shaft. The MRE is in initial contact with the shaft with the geometry provided in Table 2.2. The $\mathbf{X} = \begin{pmatrix} R & \Theta & Z \end{pmatrix}$ represent the original cylindrical coordinates of the points inside the MRE and $\mathbf{x} = \begin{pmatrix} r & \theta & z \end{pmatrix}$ represent the deformed positions.

2.3.7 Kinematics

It was assumed that a χ mapping such that $\mathbf{x} = \chi(\mathbf{X})$ exists. For the assumed mapping $\chi(\mathbf{X})$, there is a deformation gradient $\mathbf{F}$ defined as:

$$\mathbf{F} = \frac{\mathrm{d}\mathbf{x}}{\mathrm{d}\mathbf{X}} \quad \Rightarrow \quad \mathrm{d}\mathbf{x} = \mathbf{F}\mathrm{d}\mathbf{X}. \tag{9}$$

The radial, circumferential, and longitudinal stretches are $\lambda_r, \lambda_\theta$ and λ_z. Therefore, the principal stretches $\lambda_{1,2,3}$ in cylindrical coordinates [64] are:

$$\lambda_1 = \lambda_R = \frac{\mathrm{d}r}{\mathrm{d}R}, \tag{10}$$

$$\lambda_2 = \lambda_\Theta = \frac{r}{R}, \tag{11}$$

$$\lambda_3 = \lambda_Z = \frac{2z}{t}. \tag{12}$$

Thus, the deformation gradient F is:

$$\mathbf{F} = \begin{pmatrix} \lambda_1 & 0 & 0 \\ 0 & \lambda_2 & 0 \\ 0 & 0 & \lambda_3 \end{pmatrix}. \tag{13}$$

Given MREs are made of hyperelastic rubbers, their incompressibility necessitates:

$$\lambda_1\lambda_2\lambda_3 = 1 \Rightarrow \lambda_3 = (\lambda_1\lambda_2)^{-1}. \tag{14}$$

Also, the Right Cauchy-Green deformation tensor, $\mathbf{C} = \mathbf{F}^\mathsf{T}\mathbf{F}$ was obtained as:

$$\mathbf{C} = \begin{pmatrix} \lambda_1^2 & 0 & 0 \\ 0 & \lambda_2^2 & 0 \\ 0 & 0 & (\lambda_1\lambda_2)^{-2} \end{pmatrix}. \tag{15}$$

In previous studies, e.g., [65], the magnetoelastic constitutive equations of MREs are expressed in terms of the deformation invariants. The three scalar invariants of tensor $\mathbf{C}$ were obtained as [64]:

$$I_1(\mathbf{C}) = \mathrm{Tr}\mathbf{C} = \lambda_1^2 + \lambda_2^2 + (\lambda_1\lambda_2)^{-2}, \tag{16}$$

$$I_2(\mathbf{C}) = \frac{I_1(\mathbf{C})^2 - I_1(\mathbf{C}^2)}{2} = \frac{(\mathrm{Tr}\mathbf{C})^2 - (\lambda_1^4 + \lambda_2^4 + \lambda_3^4)}{2}, \tag{17}$$

$$I_3(\mathbf{C}) = \det \mathbf{C} = \lambda_1^2\lambda_2^2\lambda_3^2 = 1, \tag{18}$$

where $\mathrm{Tr}(.)$ is the trace operator. Also, three magnetoelastic invariants, $I_{4,5,6}$ were obtained according to [66] as:

$$I_4 = \mathbf{b}\cdot\mathbf{b} = \frac{a^2}{R^2} + b_Z^2, \tag{19}$$

$$I_5 = (\mathbf{Cb}).\mathbf{b} = \frac{a^2\lambda_1^2}{R^2} + b_Z^2(\lambda_1\lambda_2)^{-2}, \tag{20}$$

$$I_6 = (\mathbf{C}^2\mathbf{b}).\mathbf{b} = \frac{a^2\lambda_1^4}{R^2} + b_Z^2(\lambda_1\lambda_2)^{-4}. \tag{21}$$

2.3.8 Constitutive model

The mechanical energy was considered with the magnetic potential energy and elastic strain energy [66]. Therefore, the total potential energy function $\Omega^\star$ was:

$$\Omega^\star = \Omega + \Psi, \tag{22}$$

where Ω is the strain energy density function, and Ψ is the magnetic energy density function defined as [67]:

$$\Psi = \frac{1}{2}(\mu_0\mu_r(\zeta))^{-1}(\mathbf{Cb})\cdot\mathbf{b} = \frac{1}{2}(\mu_0\mu_r(\zeta))^{-1}I_5. \tag{23}$$

Since the MRE is mainly under compression, the principal stresses are compressive, thus, a two-term Mooney-Rivlin model was adopted. Studies have previously shown that this constitutive model

can sufficiently capture the stretch-stress behavior of hyperelastic cylinders under radial stretch [68–70]. The adopted form of Ω was:

$$\Omega = C_{10}(I_1 - 3) + C_{01}(I_2 - 3), \tag{24}$$

where C_{10} and C_{01} are the material constants of the MRE in the absence of magnetic field. It is noteworthy that for an incompressible hyperelastic material the initial shear modulus can be obtained through $G_0 = 2(C_{01} + C_{10})$. The total nominal stress tensor of MRE, combining the effects of elastic stress (due to the elastic deformation) and Maxwell stress (due to the magnetic body force) was obtained as [66]:

$$\mathbf{T} = 2\Omega_1^\star \mathbf{\Lambda} + 2\Omega_2^\star(I_1\mathbf{\Lambda} - \mathbf{\Lambda}^2) - p\mathbf{I} + 2\Omega_5^\star \mathbf{b} \otimes \mathbf{b}, \tag{25}$$

where

$$\Omega_i^\star = \frac{\partial \Omega}{\partial I_i} \Rightarrow \Omega_1^\star = C_{10}, \Omega_2^\star = C_{01}, \Omega_5^\star = \frac{1}{2}(\mu_0\mu_r(\zeta))^{-1}, \tag{26}$$

and $\mathbf{\Lambda} = \mathbf{F}\mathbf{F}^\mathsf{T}$, $\mathbf{I}$ a 3-by-3 identity matrix, p a Lagrange multiplier enforcing the incompressibility constraint, and $\otimes$ as the outer product operator such that $\mathbf{b} \otimes \mathbf{b} = \mathbf{b}\mathbf{b}^\mathsf{T}$.

Since $\mathbf{F}$ is diagonal, $\mathbf{\Lambda} = \mathbf{F}\mathbf{F}^\mathsf{T} = \mathbf{F}^\mathsf{T}\mathbf{F} = \mathbf{F}^2 = \mathbf{C}$. Therefore, the constitutive equation (Eq. 25) simplifies to:

$$\mathbf{T} = 2C_{10}\mathbf{F}^2 + 2C_{01}(I_1\mathbf{F}^2 - \mathbf{F}^4) - p\mathbf{I} + (\mu_0\mu_r(zeta))^{-1}\mathbf{b} \otimes \mathbf{b}. \tag{27}$$

The author has co-developed a solution of the equation above considering the magnetic volumetric forces on the MRE in [43] and has found the relationship between the distance between the magnets and force feedback generated by the system as:

$$F = -\xi G_\circ(1 - \lambda_1(R_i)^{-4}) - \xi(\mu_0\mu_r(\zeta)\lambda_1^2(R_i))^{-1}\left(\frac{a^2}{R_i^2}\right), \tag{28}$$

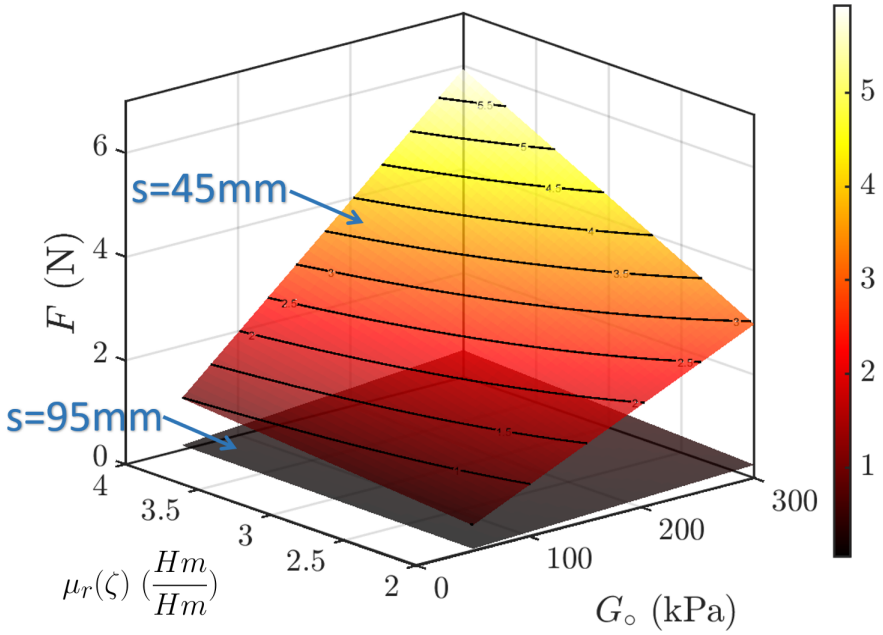

Figure 2.5: Analytical surface of force feedback with respect to variation in relative magnetic permeability and matrix's shear modulus.

where, ξ was a constant traction coefficient, and $\lambda_1(R_i)$:

$$\lambda_1(R_i) = \frac{\left(8G_0 - \Gamma_1 - \sqrt{(\Gamma_1 - 4G_0)^2 - 8G_0(\Gamma_1 + \Gamma_2)}\right)}{4G_0}, \tag{29}$$

with,

$$\Gamma_1 = (\mu_0\mu_r(\zeta))^{-1}\left(\frac{a^2}{R_oR_i}\right) - ta^2\frac{\mu_r(\zeta)-1}{\mu_0\mu_r(\zeta)}\left(\frac{1}{R_i^2} - \frac{1}{R_iR_o}\right), \tag{30}$$

$$\Gamma_2 = -(\mu_0\mu_r(\zeta))^{-1}\left(\frac{a^2}{R_i^2}\right) - a^2\frac{\mu_r(\zeta)-1}{\mu_0\mu_r(\zeta)}\left(\frac{1}{R_i^2} - \frac{1}{R_iR_o}\right). \tag{31}$$

Eq. 28 explicitly related the variation of force feedback F and $\mu_r(\zeta)$ and $G_\circ$. This relationship is highly nonlinear and was exploited to show the trend of variation of the force range with the variation in ζ and $G_\circ$. It is noteworthy that with any given $(G_\circ, \xi)$, a specific force range (F_{min}, F_{max}) was obtained which corresponded to (s_{max}, s_{min}), where $s_{min} = 45$mm. Fig. 2.5 shows two extreme surfaces of force range with CIP percentage (ζ) and shear modulus $G_\circ$. The distance between the two surfaces presented in Fig. 2.5 shows the analytical force range of the force feedback device. As a representative working point, $\mu_r = 4$ and $G_\circ = 277$kPa is similar to the working point that

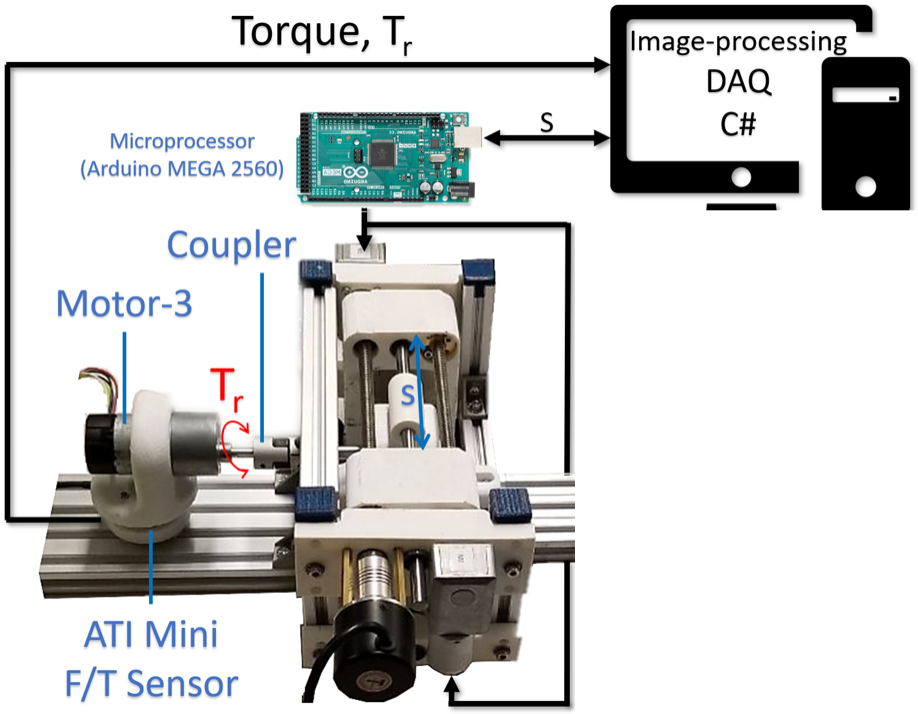

Figure 2.6: Experimental setup used in the validation study.

the prototype in our previous study [43]. The experimental force range in [43] was 0.5–5.7 N while Fig. 2.5 indicates a force range of 0.46–5.4 N. Moreover, the findings suggest that increasing the permeability and increasing the shear modulus both increase the force range (difference between the two surfaces in Fig. 2.5). This finding also suggest that with proper selection of matrix polymer ($G_\circ$) and CIP percentage (ζ), different force ranges can be attained. Such feature is desirable for adapting the proposed force feedback modality for various applications, such as RCI (0–2 N), general surgery (0–5 N) and eye surgery (0–0.5 N) as representatives.

2.4 Validation Study

2.4.1 Protocol

The objective of the validation study was to measure the force range of the force feedback system with the fabricated MREs to investigate the effect of CIP percentage and matrix shear modulus. To this end, the experimental setup shown in Fig. 2.6(a) was used. In the setup, the shaft of the

device was connected to Motor-3, a 12v DC motor (37D-4754, Polulu Robotics and Electronics, NV, USA), using zero-backlash Oldham-type coupler (9845T57, McMaster-Carr, IL, USA) for running in continuous rotation(20 rpm) [71]. Also, a 3D-printed base was fabricated to align the motor with the shaft and to house an ATI-Mini40 force sensor (SI-20-1, ATI Inc., MD, USA). The sensor was utilized to measure the torque generated by the motor to maintain its rotational speed. The measured torque is a surrogate of the transmissible haptic force with the ratio coefficient of ξ. With each MRE, the gap distance between the magnets was set to $s = 45$mm and $s = 95$mm to determine the minimum and maximum generated force feedback.

2.4.2 Results

2.4.2.1 Analytical force range

For the verification of the proposed analytical model, the estimated force range by the analytical model were compared with the experimental results. Table 2.4 compares the estimated force range and experimental findings. As the comparison suggests, the analytical estimation were in fair agreement with the experimental observations. The maximum relative error of the analytical model was 14.7% for MRE-50-30, while the average force range estimation had a relative error of 10.2%. This finding shows improvement of the force range estimation in this study compared to [43], where a maximum relative error of 26% was reported for similar MREs. The analytical model has overestimated the force range (except for MRE-10-20, MRE-10-30, and MRE-40).

2.4.2.2 Effect of shear modulus (Matrix)

Fig. 2.7(a) shows the variation of resistant torque MRE-50-40, MRE-30-30, and MRE-10-20 as three representatives. In this figure, the force feedback shows step changes as a result of step-wise decrement in the gap between the magnets, whereas, the minimum force feedback was observed for $s = 95$mm and maximum force feedback was observed for $s = 45$mm. The intermediate steps were sequentially corresponding to $s = 85, 75, 65,$ and 55. For the sake of comparison with the proposed analytical model, the maximum and minimum force feedbacks were estimated from Eq.

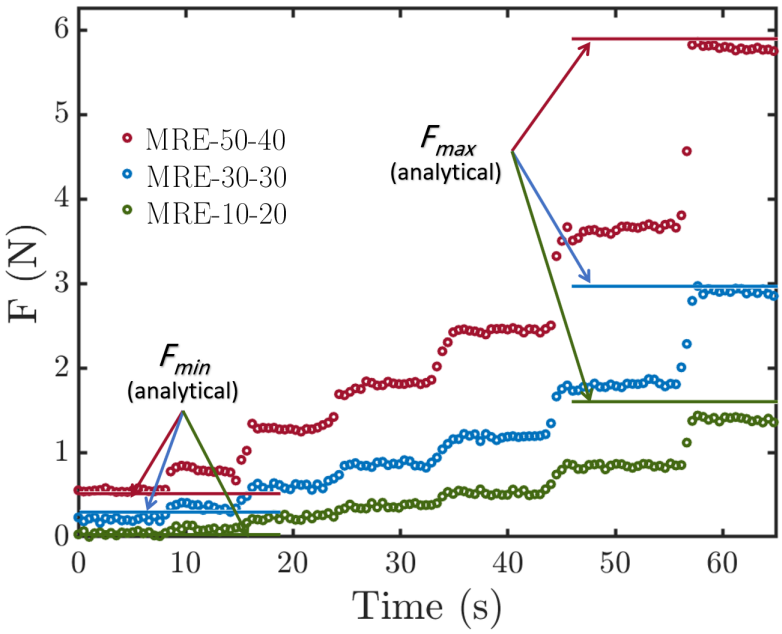

(a)

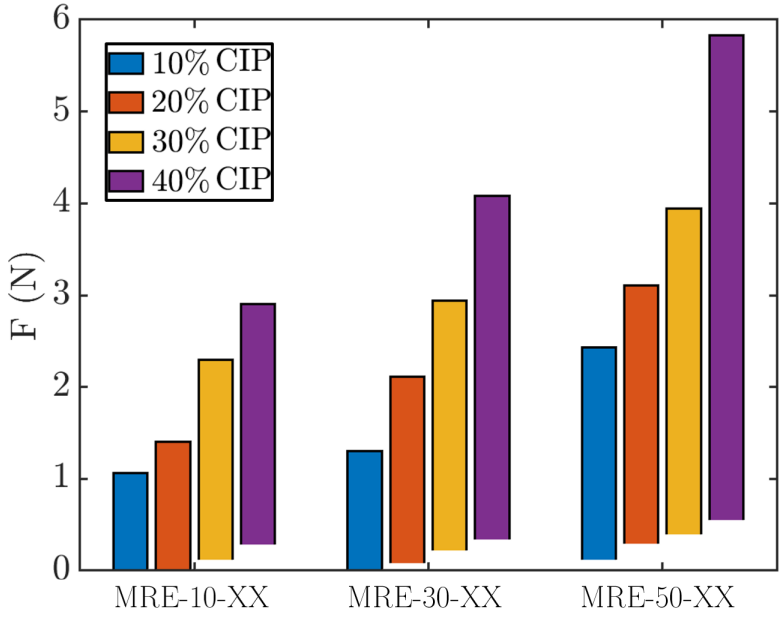

(b)

Figure 2.7: (a) Variation of force feedback with changes in the gap distance between the magnets for three representative MREs and (b) variation of maximum and minimum force feedback with CIP percentage, and matrix shear modulus.

Table 2.4: Comparison of analytical estimation versus experimental force feedback range.

MRE	$G_\circ$ (kPa)	CIP (%)	Force range (Analytical) (N)	Force range (Experiment) (N)	Error (Abs.,Rel.)* (N,%)
MRE-10-10	79.5	10	1.11	1.06 ± 0.18	0.05, 4.7
MRE-10-20	106.4	20	1.34	1.40 ± 0.11	0.06, 4.3
MRE-10-30	139.9	30	2.07	2.19 ± 0.13	0.12, 9.2
MRE-10-40	175.0	40	2.42	2.63 ± 0.23	0.21, 8.0
MRE-30-10	87.2	10	1.46	1.34 ± 0.12	0.16,12.3
MRE-30-20	120.1	20	2.31	2.04 ± 0.22	0.27,13.2
MRE-30-30	144.8	30	2.98	2.73 ± 0.20	0.25, 9.2
MRE-30-40	188.5	40	4.14	3.76 ± 0.15	0.39,10.4
MRE-50-10	88.9	10	3.10	2.77 ± 0.17	0.33,11.9
MRE-50-20	137.6	20	3.23	2.83 ± 0.09	0.40,14.1
MRE-50-30	185.5	30	4.16	3.55 ± 0.20	1.23,14.7
MRE-50-40	277.3	40	5.82	5.29 ± 0.14	0.53,10.0
Mean	–	–	–	–	–, 10.2%

*Abs.: Absolute error.
*Rel: Relative error.

28 and depicted on Fig. 2.7(a).The force feedback F was calculated as:

$$F = \xi ||\mathbf{T}_r||, \tag{32}$$

where, $||\mathbf{T}_r||$ was the total resistant torque measured by the ATI Mini40 force sensor. Comparison of the experimental results with the analytical estimations for all the MREs showed an average difference of 0.17 ± 0.09 N for F_{max} and 0.066 ± 0.04 N for F_{min}.

Another finding was that both the minimum and maximum force feedback increased with increasing the shear modulus of the matrix. However, the increase in the maximum force was greater than the increase in the minimum force, thus resulted in increasing the total force feedback range, i.e., $F_{max} - F_{min}$. Fig. 2.7(b) compares the force feedback range amongst the MREs.

2.4.2.3 Effect of CIP content (Filler)

The experimental onservations showed two distinct effects for increasing the CIP contents in the MREs. The first observation was that increasing the CIP content resulted in increasing the shear

modulus of the MREs. As summarized in Table 2.3, increasing the CIP content from 10% to 40% increased $G_\circ$ of MRE-10-XX, MRE-30-XX, and MRE-50-XX by 120%, 116%, and 211%, respectively. As predicted by the analytical model(Fig. 2.5), increasing $G_\circ$ alone would increase the force feedback range. Meanwhile, increasing the CIP content would increase the relative magnetic permeability, μ_r, that would also boost the increase in the force range. The increase in the CIP content from 10% to 40% resulted in increasing the force range of MRE-10-XX, MRE-30-XX, and MRE-50-XX by 1.57N (248%), 2.45N(288%), and 2.52N(190%). Despite higher F_{max} in MRE-50-XX, the change in the force range with CIP was only 0.1N larger than MRE-30-XX. This phenomenon was related to the increase in the F_{min} that compromised the force range by increasing the lower force band. Similar pheonomenon has been reported in [43]. The reason for having non-zero F_{min} with CIP content of 30% and 40% is that with such CIP content, the relative permeability of the MREs is high enough to generate large magnetic field intensity within the MRE even at the minimum magnetic fields generated with $s = 95$mm. Such magnetization consequently generates residual stress within the MRE and results in non-zero minimum force feedback.

One of the mitigation measures for avoiding non-zero F_{min} would be to redesign the structure of the device such that allows for higher maximum gap separation between the magnets.

2.4.2.4 Force ranges and applications

For the sake of comparison with other proposed force feedback rendering, Table 2.5 summarizes representative studies in the literature with their reported force ranges and comparison with the proposed MREs in this study. As the comparison suggests, for each of the representative studies there is at least one MRE that can generate comparable force range. This comparison suggest the versatility of the proposed device and MREs for various surgical robotics applications. It also implies that with the proposed device and MREs, researchers can have one single force feedback system with a assortment of MREs that meet the force range requirements for various applications. The fact that the proposed design of the MRE mold and direct assembly with the device facilitates rapid and easy installation of various MREs in the device

Table 2.5: Comparison of the force range of the MREs in this study with representative force feedack applications in the literature.

Study	Application	Force Range	Comparable MRE	MRE Force Resolution
Yu *et al.* [72] (2021)	Cardiovascular	0–1.4	MRE-10-20	7 mN
Azarnoush *et al.* [73] (2016)	Brain	0–0.3	MRE-10-10	5 mN
Masaki *et al.* [74] (2021)	Broncoscopy	0–0.5	MRE-10-10	5 mN
Zuo *et al.* [75] (2021)	Viteroretinal	0–0.2	MRE-10-10	5 mN
Wottawa *et al.* [76] (2016)	Laparoscopy	0–3.4	MRE-30-30 MRE-50-30 MRE-50-40	15 mN 20 mN 29 mN

2.5 Summary

The objective of this study was to investigate the effect of CIP percentage and shear modulus of the matrix in the force feedback range of the proposed device in [43]I. To this end, first a constitutive model of MREs was adopted and augmented with a variable magnetic permeability term to model the variation of force feedback with CIP percentage and shear modulus of matrix. The validated analytical model can be used in future studies to simulate the force feedback rendering or to predict the performance of other MREs. Afterwards, twelve MREs with various CIP percentages and shear moduli were fabricated, characterized, and tested for their initial shear modulus and force feedback range in the proposed haptic feedback system. The results showed fair agreement between the analytical force ranges estimations and experimental observations. Also, the force range of MREs covered a fairly large force range that would meet the requirements of various surgical robotics applications.

In future studies, the validated parameteric constitutive model could be used for structural optimization of the proposed haptic device and MRE dimensions. This study was limited to the investigation of the elasticity and magnetism of the MRE, while the shape and size of the MRE can influence the force range (as predicted by Eq. 28). Another potential extension of this work would be to investigate the force ranges of the MREs for specific robotic surgery tasks, similar to [43], to demonstrate the feasibility of rendering task-specific force feedback. Similarly, the proposed MREs have the

potential to be used as tactile media to be used with magnetic-based tactile displays, e.g., [30, 57]. Another possibility would be to study the feasibility of simultaneous force (or torque) sensing with the MRE. MREs have been recently successfully used for sensing applications [56, 77].

Chapter 3

Structural Optimization of a Magnetostriction-based Force Feedback System for Telerobotic Intervention

Robot-assisted cardiovascular intervention (RCI) has faced adoption challenges. One of the limitations of the RCI systems is the lack of haptic feedback. Previously, the author has proposed and validated the feasibility of a novel smart material-based haptic rendering system for RCI applications, i.e. TorMag. However, state-space analysis of TorMag showed its suboptimal performance in terms of achieving total coverage of the required force rendering range for robot-assisted cardiovascular tasks. To alleviate this limitation, structural optimization of the proposed system based on magnetoelastic modeling and with global optimization was performed. To this end, the performance of the system was reconstructed in the force state-space. Afterward, a multi-variable goal function was proposed to maximize the coverage of the state-space of the haptic system with the required state-space. Four design parameters, i.e., thickness, the outer radius of the magnetorheological elastomer, and maximum separation distance of the permanent magnets were considered. The minimization problem was solved using the Marquard-Levenberg algorithm in Matlab R2021a. As representatives, the optimization was performed for two different required state-spaces. In each case, the global optimality was obtained by using multiple initial guesses. The results showed that

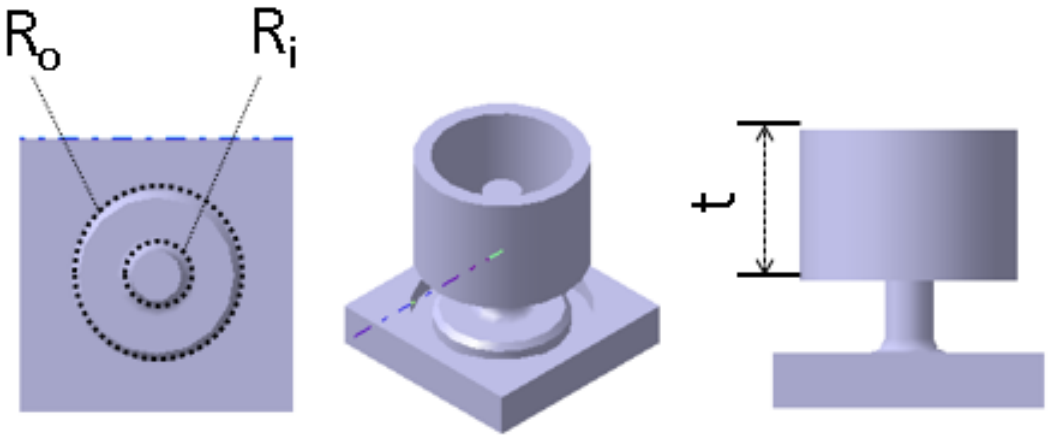

Figure 3.1: Dimensions and the design of the mold for the MRE component.

the optimized design increased the state-space coverage from 88% and 91% to 100% in both representative tasks.

3.1 Study Objectives

The objective of this study was to optimize the geometrical design of the MRE and TorMag to improve the range of rendered forces so as to match the exhibited phase portrait of TorMag with the required phase portrait of RCI applications.

3.2 Related Studies

Recently, the author co-developed a new force feedback modality for RCI applications based on frictional torque generation between a ferromagnetic shaft and a hollow cylindrical MRE [43]. The MRE-based system (TorMag) exhibited acceptable compliance with the functional and physical requirements of haptic displays for robot-assisted surgery. However, the experimental results showed non-optimal force phase portrait coverage compared to experimental force feedback phase portrait for RCI applications. The reason for that was non-optimized structural design of the MRE and insufficiency of the maximum feasible separation between the two magnets. Therefore, this study is aimed at proposing an model-based optimization method for obtaining the optimized values of MRE dimensions and maximum feasible magent separations to comply with phase-portrait of two

representative RCI tasks that are obtained experimentally in [43]. The force-separation relationship for TorMag is [43]:

$$F_r = -\xi G_0(1 - \lambda_1(a, R_i)^{-4}) + \xi(\mu_0\mu_r\lambda_1^2(a, R_i))^{-1}\left(\frac{a^2}{R_i^2} - b_Z^2\right) \tag{33}$$

where F_r is the haptic force generated by the frictional torque at the interface of the output shaft and MRE and ξ is the traction coefficient defined as:

$$\xi = \frac{\lambda_3(R_i)2\pi t R_i^2 \mu_d}{R_w}, \tag{34}$$

with $R_w = 20mm$ the roller radius inside the catheter insertion system. Eq. 33, relates the geometrical dimensions R_i, R_o, and t, that are the inner radius, outer radius and thickness of MRE mold, respectively. Also, the maximum distance between magnetic plates s_{max} is the fourth parameter that affects the performance of TorMag. The minimum feasible force in TorMag is directly dependent on s_{max}. The causality is that at s_{max} the MRE is subjected to the least magnetic field thus generates the lest force. More specifically, parameter a is a fitting heuristic that determines the variation of the strength of the radial magnetic field within the MRE. This parameter changes with the distance between the two magnets such that:

$$a(s) = c_1(s_{max} - s)^p + c_2 \tag{35}$$

In previous study, the empirical values of c_1, c_2, and p were 1.206, 1256, and 1.867, respectively. It was observed that s_{max} =95mm in the initial design was not large enough to generate near-zero forces [43]. The geometrical parameters and the design of the mold used for fabricating the MRE component are shown in Fig. 3.1. Also, Table 3.1 summarizes the dimensions of TorMag for RCI applications. In this study a structural optimization method is proposed to optimize the performance of TorMag to increase its state-space coverage for RCI tasks.

Table 3.1: Initial geometrical dimensions of TorMag for RCI application.

	MRE Cylinder			Shaft	Housing		
Dimension	R_i	R_o	t	l_s	l_1	l_2	l_3
(mm)	4	11	20	75	40	45	40

3.3 Material and Methods

3.3.1 Problem Definition

The MRE emulsion is poured in the mold and MRE mold is placed in MRE hub. MRE holder could be easily inserted in and removed from the inner compartment of TorMag. Then an iron shaft between TorMag and RCI system is inserted to the TorMag as shown in Fig.2.1. The friction between MRE and shaft produces a resistant torque (T_r) which will be converted to insertion force F in the RCI system. In RCI application, the phase portrait has a trapezoid form illustrated in Fig. 3.2. The phase-portrait illustrates the variation of the generated force with rate of change in the force. The phase portrait of TorMag was obtained by analytical derivation of the force (F_r in Eq. 33) and force rate ($\dot{F}_r = \frac{\mathrm{d}F_r}{\mathrm{d}t}$). The force rate was analytically obtained as follows:

$$\dot{F}_r = \frac{\mathrm{d}F_r}{\mathrm{d}s}\dot{s} = \left(\frac{\partial F_r}{\partial a(s)} + \frac{\partial F_r}{\partial \lambda_1(a, R_i)}\frac{\partial \lambda_1(a, R_i)}{\partial a(s)}\right)\frac{\mathrm{d}a(s)}{\mathrm{d}s}\dot{s}. \tag{36}$$

On the other hand, $\dot{s}$, the velocity at which TorMag changes the gap distance between permanent magnets, was obtained by using the TorMag's PID controller performance reported in [43]. The rise time t_r of the PID controller in TorMag for 1mm change in the gap was 0.12s, thus:

$$\dot{s} = \frac{\mathrm{d}s}{\mathrm{d}t} \approx \frac{\Delta s}{\Delta t} = \frac{1\mathrm{mm}}{t_r} = 8.333\frac{\mathrm{mm}}{\mathrm{s}}. \tag{37}$$

Therefore, upon substituting $a(s)$ and $\dot{s}$, Eq. 36 simplified to:

$$\dot{F}_r = \Gamma(R_i, R_o, t, a, s)(8.33c_1p(s_{max} - s)^{p-1}), \tag{38}$$

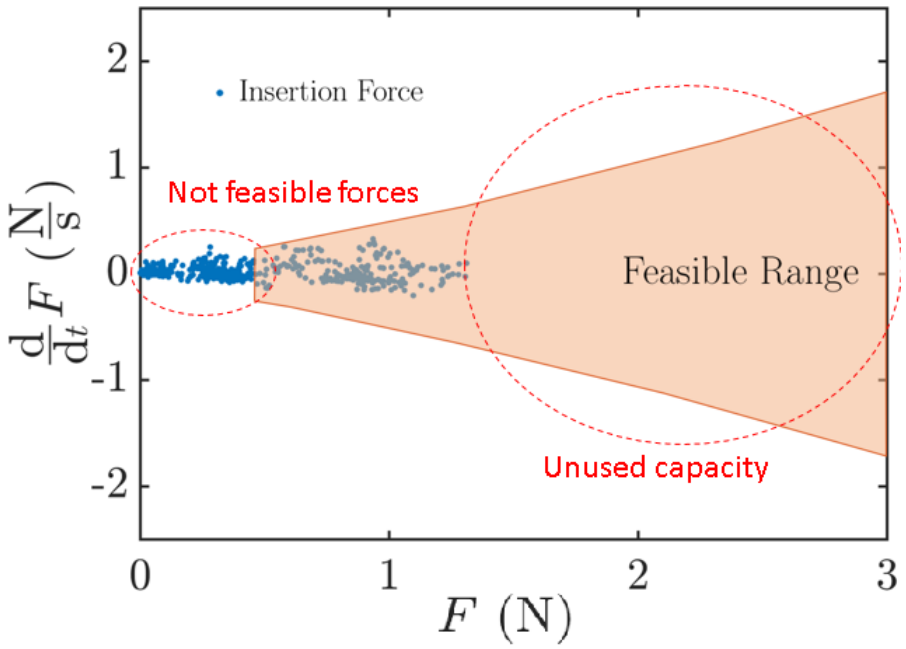

Figure 3.2: Comparison of the phase-portraits of the deired force (the measured insertion force at the patient unit) with the feasible force generation area of +TorMag in aorta cannulation.

where, Γ is the magnetoelastic characteristic function embedding the effects of design parameters R_i, R_o, t.

Eq. 33 and Eq. 38 were used to illustrate the phase portrait of TorMag with initial design. Eq. 33 and Eq. 38 were used to optimize the design parameters to attain the desired feasible ranges.

Table 3.2: Comparison between initial guess and optimized solution.

	Initial guess			Initial coverage	Optimized dimensions			Optimized coverage
	R_o (mm)	t (mm)	s_{max} (mm)	(%)	R_o (mm)	t (mm)	s_{max} (mm)	(%)
Use-case 1	11	20	95	88%	15	30	85	96%
	12	23	140	88%	14	30	87	100%
	14	23	200	88%	15	32	85	100%
	9	35	175	88%	15	30	85	99%
	8	45	60	88%	14	29	85	97%
Use-case 2	11	45	95	91%	14	29	138	94%
	7	27	150	91%	14	29	187	100%
	7	30	150	91%	15	28	145	97%
	40	50	170	91%	15	29	165	99%
	20	15	100	91%	15	30	200	100%

Fig.3.2 shows a representative related phase portrait of TorMag and compares it with experimental state-space points adopted from [43]. The MRE used in [43] was of G_0=300 kPa and μ_r=3.8. It was observed that some working points in the experimental data were out of trapezoid area. This led to insufficiency of TorMag to generate small forces while it had unused force capacity at higher forces for the RCI application. The reason of this problem was that the dimensions used in the initial design (Table 3.1) were arbitrary to show the feasibility of the concept and were not optimized. Thus, this study was aimed at finding optimized structural dimensions for TorMag components so that its feasible force generation range covers the desired experimental working points on the phase portrait.

3.3.2 Structural Optimization

Fig. 3.3 shows the non-optimized (initial) and desired performances in phase portrait space. In order to tune design parameter to achieved the desired performance a minimization problem was defined. The goal function to minimize was defined as the distance between four corners of the phase portrait of TorMag and their corresponding points in the desired performance. The distance vectors were labeled as d_1, d_2, d_3 and d_4 and are representatively shown in Fig. 3.3. The goal function $\Lambda(R_o, t, s_{max})$ was defined as:

$$\Lambda(R_o, t, s_{max}) = \sum_{i=1}^{4} ||\mathbf{d}_i||^2 = ||\mathbf{d}_1||^2 + ||\mathbf{d}_2||^2 + ||\mathbf{d}_3||^2 + ||\mathbf{d}_4||^2. \quad (39)$$

Referring to the physical conditions, R_i is equal to radius of the output shaft of the TorMag with a fixed value of $4mm$. Thus, R_i was not considered among the geometrical parameters. Therefore, the design parameters included in the optimization were R_o, t and, s_{max}.

For the optimization, two use-case tasks were considered as representatives. The experimental data on the use-cases were adopted from [43]. For each representative task, the required performance was manually defined so that the resulting trapezoid would cover the experimental state points on the phase portrait. The optimization was performed in Matlab R2021a (Mathworks, MA, USA) using constrained optimization technique. The design constraints were obtained from physical and

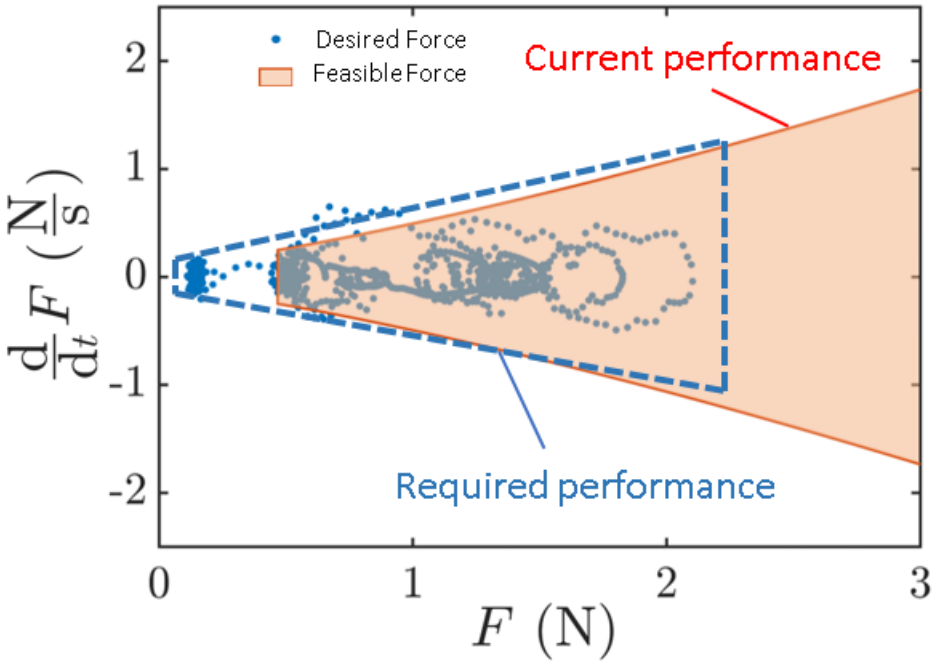

(a)

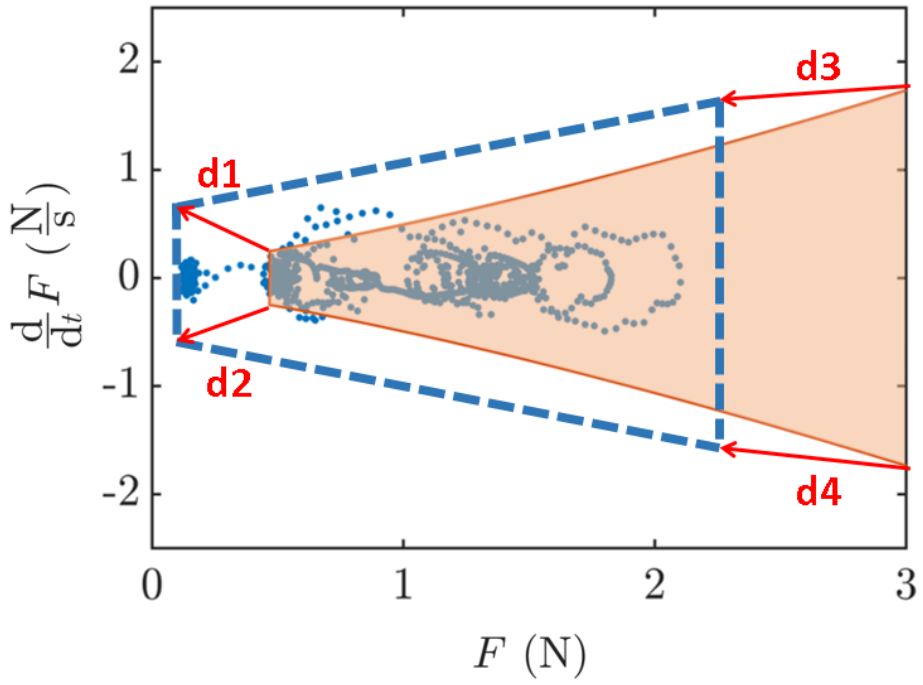

(b)

Figure 3.3: (a) Comparison between the current TorMag performance in phase portrait with the desired forces from experimental data in [43], (b) graphical representation of the goal function parameters $\mathbf{d}_{1\text{–}4}$ on the phase portrait.

manufacturability conditions and were as follows:

$$C_1 : 6.5\text{mm} < R_o < 45\text{mm} \tag{40}$$

$$C_2 : 0.5\text{mm} < t < 50\text{mm} \tag{41}$$

$$C_3 : 45\text{mm} < s_{max} < 200\text{mm} \tag{42}$$

The rationale for C_1 and C_2 was that the shell thickness and length of the MRE, i.e. $R_o - R_i$ and t, should not be less than 0.5mm due to manufacturability considerations. Also, C_3 was imposed because $s_{max} \leq 45$mm would physically interfere with the MRE hub design and was not feasible and for $s_{max} \geq 200$mm the haptic force would effectively drop to zero.

In addition, for global optimality, each representative case was solved for five random initial guesses and the minimum of the minima was selected as the global optimum.

3.4 Results and Discussion

Table 3.2 summarizes the optimized dimensions of TorMag and the phase portrait coverage for the two representative use-cases. The reported initial coverages correspond to the dimensions of the original TorMag design summarized in Table 3.1. It was observed that the initial guess affected the optimized coverage percentage that justified the use of global optimality for this problem. Also, in both cases, the optimization procedure was successful in finding a feasible solution for total coverage, i.e., 100%. Fig. 3.3 depicts the optimized phase portrait coverage for the two representative use-cases.

The results also showed that s_{max} was a critical factor in enabling the system to render zero force condition. In addition the optimization increased the phase portrait coverage to 100% from 88% and 91%, in use-case 1 and 2, respectively which are corresponding to 13.6% and 10% increase in the dynamic performance of the TorMag.

Also, it was observed that the optimization obtained an $R_o = 15$mm for both use-cases. Comparing with $R_i = 6mm$ the optimal shell thickness of the MRE was obtained to be 9mm. The optimized value of t was also similar for both use-cases, i.e. $t = 30$mm. Given that the initial guesses for

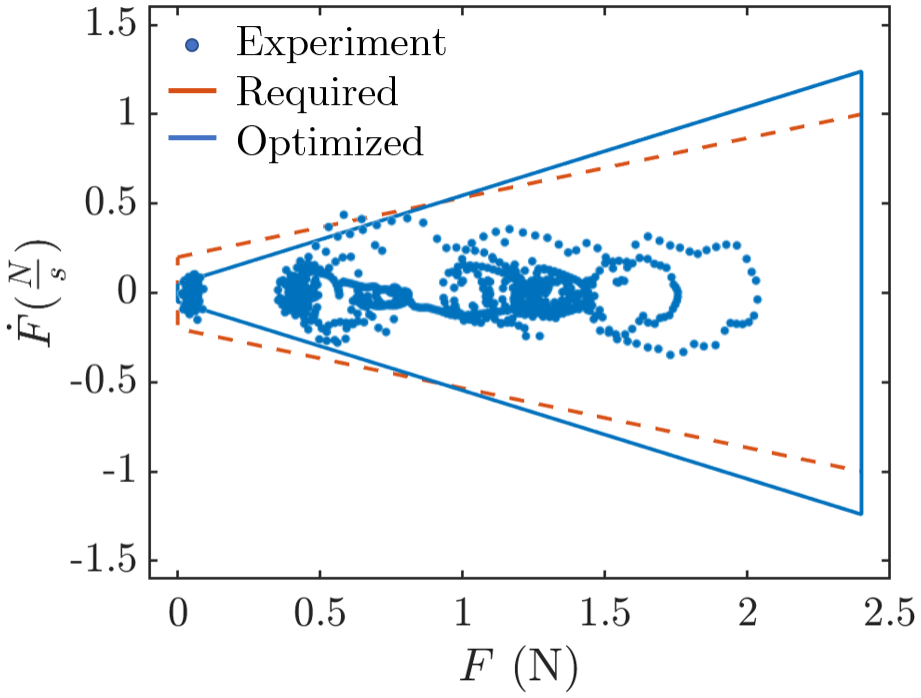

(a)

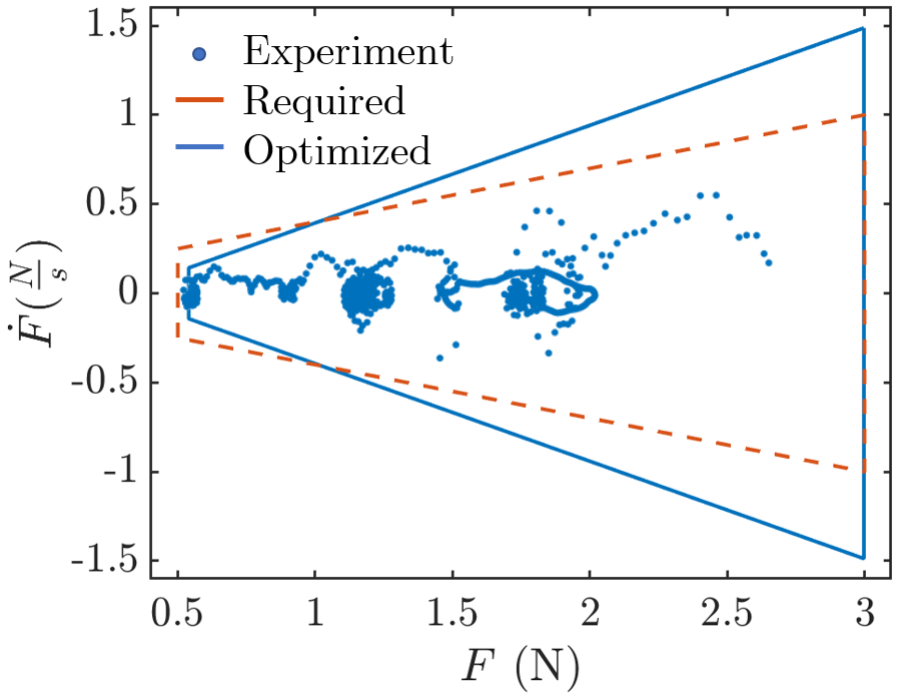

(b)

Figure 3.4: Comparison of the optimized performance with the required performance and experimental data for use-case 1 and use-case 2.

R_o and t used in the optimization process varied for five repetitions in each use-case, the author rule-out the possibility of optimizer stagnation at the initial guess. The reason might be related to difference in the contributions of the design parameter R_o and t with the contribution of s_{max} to the performance in phase portrait. As depicted in Fig. 3.4, the maximum required force (blue points) is approximately 2.5 N and 3 N for use-case 1 and use-case 2, while the minimum force is 0 for use-case 1 and 0.5 N for use-case 2. Thus, R_o and t contribute to fulfilling the maximum required force and given somewhat similarity in both use cases for maximum force, their optimized values are similar. However, s_{max} merely contributes to the minimum achievable force and given the difference in the two use-cases the optimize values for s_{max} are different. Also, the reason for large difference in the optimized value of s_{max} for use-cases is that as s_{max} increases, the ability of the permanent magnets to change the radial magnetic field diminishes (inverse relationship was observed and verified in [43]). In other words, the sensitivity of radial magnetic field to the separation between the magnets decreases while s_{max} increases. Thus, relatively large s_{max} is required to enable TorMag rendering near-zero forces.

During the optimization it was observed that the optimizer would first fulfill the maximum required force and next fulfill the minimum required force. This shows that the gradient of the goal function with respect to R_o and t was larger than its gradient with respect to s_{max}. Moreover, the proposed goal function was smooth and converged during all the optimization solutions, i.e., for 10 initial guesses. Therefore, this goal function can be exploited to include other non-geometric design parameters such as G_0 to fine-tune other design parameters. This approach can further be utilized to fabricate special MREs for different applications such as neurovascular or robot-assisted bronchoscopy. Given that TorMag is of modular design, it can be accompanied with various MRE inserts to be used for different surgical applications.

3.5 Summary

In this study, structural optimization of a force feedback system based on its magnetoelastic model was investigated. The results showed that the proposed method was successful in finding a feasible optimized design for the force feedback system. Also, since the proposed goal function was based

on the system performance in the phase portrait it could capture the dynamic response of the system and eventually resulted in feasible dynamics for the system. Similar approach can be adopted for future studies to design other MREs and optimized dimensions for other surgical tasks, e.g., neurovascular intervention and robot-assisted bronchoscopy.

Chapter 4

Modeling of Rate-dependent Force-Displacement Behavior of MREs using Neural Networks for Torque Feedback Applications

Magnetorheological smart elastomers exhibit controllable properties in the presence of controlled external magnetic field. Recently, such elastomers have been used for tactile display applications. In this study, a control framework for TorMag system was proposed. As a necessary block in the proposed control framework, a model to obtain the required magnetic field to achieve a desired force-displacement behavior was required. To this end, a neural network-based model was proposed and validated. Also, a search methods based on the nearest neighbor approach was proposed and its performance to predict a desired force profile was assessed with referende to the available experimental data. The proposed neural network was accurate in predicting the force-displacement behavior of three types of MREs ($R^2 = 0.97$, mean-absolute-error=1.26 N). Also, the proposed search method was successful in obtaining the required magnetic field to demonstrate a desired force-displacement profile (mean-absolute error=3.64 mT). The proposed learning-based MRE model and search method showed favorable performance for incorporation to the proposed

torque control framework.

4.0.1 Study Objectives

In this study, the author has proposed a learning-based modeling method for mechanical behavior of MREs with application in torque feedback applications. This study was aimed at finding a data-driven model to find the required magnetic field for observing a desired force-displacement behavior. A desired force-displacement curve (for shear mode) can be used to control the torque applied on a shaft with a given torsional displacement. To this end, a non-parametric neural network (NN)-based model for predicting the behavior of the MREs was developed using the experimental data available from [57]. Furthermore, as a prerequisite for control of force-displacement, an iterative nearest neighbor search (NNS) method was proposed for finding the magnetic field required for obtaining a desired force at a given displacement. In the end, the accuracy of the NN-based prediction and control was studied for a force tracking task.

4.1 Related Studies

To model the mechanical behavior of MREs, mechanistic and heuristic approaches have been proposed in the literature. Young *et al.* [78] used a non-parametric ant colony algorithm for this purpose. Their model was fairly accurate for monotonic loading conditions however was not accurate in capturing the hysteresis response. In another study, Leng *et al.* [79] proposed an fuzzy optimized NN for capturing the viscoelastic behavior of MREs under shear loading. Their results have shown superior accuracy compared to the conventional parametric Bouc–Wen models. Dargahi *et al.* [44] presented a parametric Prandtl-Ishlinskii model for capturing the nonlinear hysteresis properties of MREs. Their proposed model utilized a large number of heuristic parameters and is parameter sensitive. Therefore, temporal changes in the properties of the MREs may introduce large prediction errors. In another study, Vatandoost *et al.* [80] introduced an artificial neural network (ANN) with back-propagation training technique for prediction of the dynamic behavior of MREs in tension-compression mode. Their model was fairly accurate in predicting the force-displacement response of the MREs.

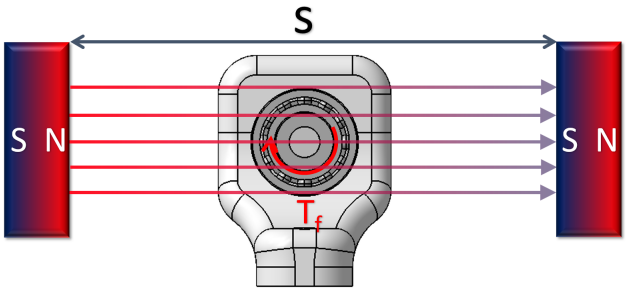

(a)

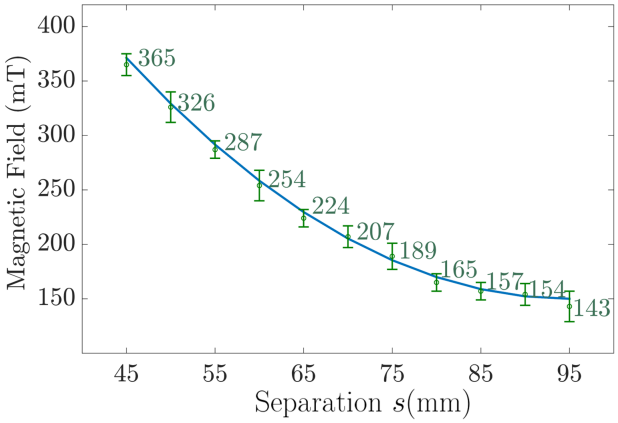

(b)

Figure 4.1: (a) TorMag under magnetic field generated by two permanent magnets, (b) the change of the average magnetic fields within the MREs.

4.2 Material and methods

By controlling the external magnetic field on the MREs, the induced magnetic field within the central shaft changes which changes the state of magnetic body force on the MREs (magnetic pull). This configuration would result in increasing the frictional contact force between MREs and central shaft with increasing the external magnetic field and vice versa. Therefore, in order to obtain a desired friction-induced resistant torque on the central shaft a specific external magentic field intensity is required.

4.2.1 Proposed Torque Control Framework

Fig. 4.2 depicts the proposed torque control framework for TorMag described in Sec. 4.2. Finding the desired magnetic field for a desired torque (force) is an inverse problem. Previously proposed parametric models cannot be solved inversely to find the desired magnetic field due to the complexity and heuristic nature of such models. Therefore, in the following an NN model is proposed and is coupled with an NNS optimization model to find the desired magnetic field. The scope of the proposed methods in this study is shown with the shaded area in Fig. 4.2.

4.2.2 Magnetic Field Generation

As depicted in Fig. 4.1(a) the external magnetic field was generated using two permanent magnets held at a distance s. As described in [30], utilization of a permanent magnets is more favorable for this study as, unlike magnetic coils, it does not require constant electric current feed, thus is a passive magnetic field generation method. Using two Neodymium N52 permanent magnets (CMS Magnetics Inc., TX, USA) the author observed average magnetic field in the range of 0–365 mT within the MREs [57] (Fig. 4.1(b)).

4.2.3 MRE Classes

The MREs used in this study were developed by the author in [30]. The MREs were composed of EcoFlex 00-20 (Smooth On Inc., PA,USA) Silicon rubber as matrix and Cabonyl iron particles (CIPs) as filler. Three force-displacement curve of three classes of MREs with 25%, 35%,

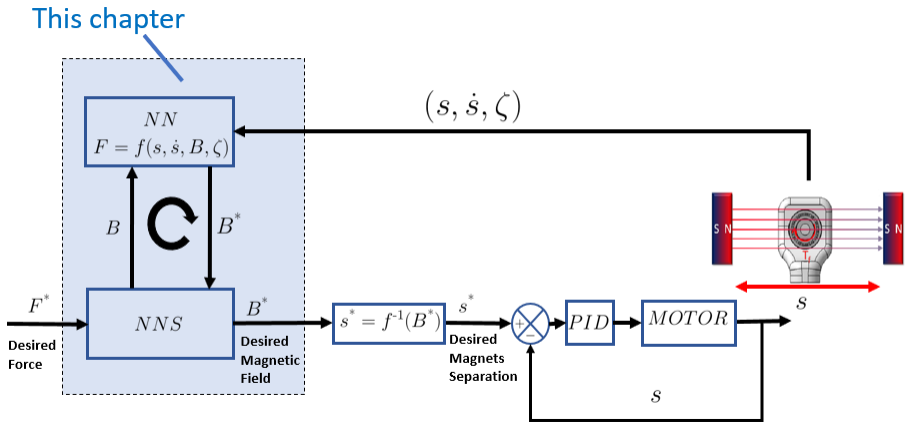

Figure 4.2: Proposed torque control framework for the proposed MRE-based torque feedback system. The scope of this study is shown with the shaded area.

45% volume-fraction of CIP were investigated in this study. These classes are denoted as MRE-A, MRE-B, and MRE-C hereinafter. The average elastic modulus of MREs A, B, and C in uniaxial compression in the absence of magnetic field were 81 kPa, 183 kPa, and 281 kPa which changed changed nonlinearly to 130 kPa, 341 kPa, and 592 kPa at 365 mT [57].

4.2.4 Force–Displacement Characteristics of MREs

Fig. 4.3(a-c) depicts the force displacement characteristics of the MRE-A, MRE-B and MRE-C based on the data reported in [57]. It was observed that the MREs exhibited different behavior during loading and unloading (hysteresis). This shows that the mechanical behavior of MRE is rate-dependent. Therefore, similar response is anticipated and has been shown for shear loading mode [60]. Moreover, the stiffness of MRE-A, B and C at similar magnetic fields increased as with their CIP percentage increases. The same increasing trend was observed for each MRE as the external magnetic field increased. These observations were crucial in selecting the features vector used for training the NN.

4.2.5 NN-based Modeling of MREs

In order to model the relationship between force, displacement, and magnetic field the intuition obtained from observations described in 4.2.4 was used. The components of the features (input) vector were selected as displacement s, rate of displacement $\dot{s}$, magnetic field B, and CIP content

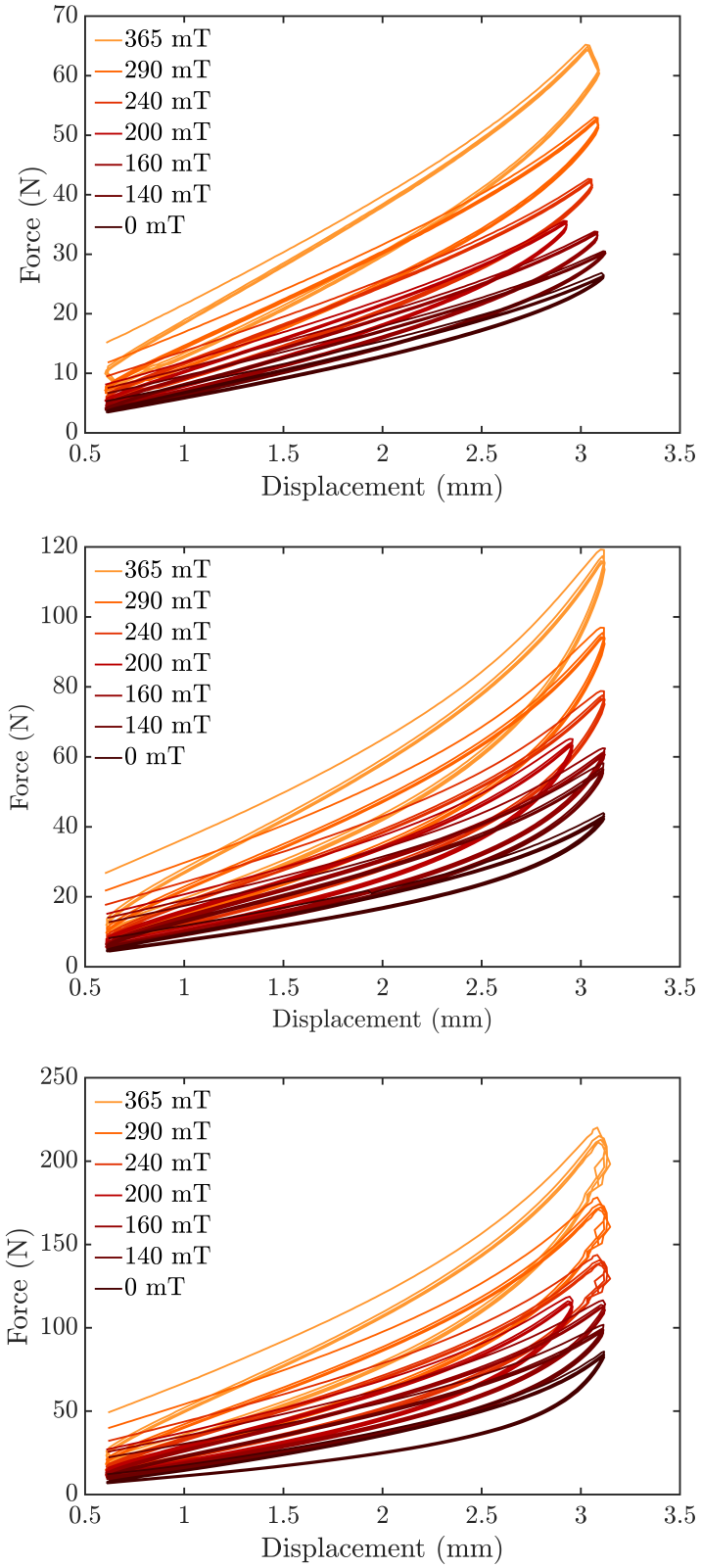

Figure 4.3: Force–displacement characteristic of MRE-A, MRE-B, and MRE-C under various magnetic fields.

Table 4.1: Performance metrics for the NN predictions.

	Training dataset			Test dataset		
	MAE (N)	MAE%	R^2	MAE (N)	MAE%	R^2
MRE-A	0.50 ± 0.41	0.99	0.99	0.62 ± 0.54	0.95	0.99
MRE-B	1.03 ± 0.91	0.99	0.99	1.44 ± 1.02	1.02	0.98
MRE-C	1.85 ± 1.33	1.21	0.96	2.7 ± 2.21	1.45	0.94
All	1.15 ± 0.98	1.04	0.97	1.26 ± 1.05	0.95	0.97

ζ. Also, force F was considered as the output vector. The experimental dataset from Fig. 4.3 contained $69,300$ tuples of data (input x and output y) with the form:

$$x = \begin{pmatrix} s_i & \dot{s}_i & B_i & \zeta_i \end{pmatrix}, \quad y = \begin{pmatrix} F_i \end{pmatrix}, \tag{43}$$

with $i = 1, 2, \cdots, 69300$. The dataset was randomly splitted into training and test datasets with a ratio of $70:30$.

A feed-forward three-layer NN with one input layer (four neurons), one hidden layer (50 neurons), and one output layer (one neuron) was found to be sufficient to capture the force-displacement behaviors. A sigmoid activation function was used between the hidden layer and output layer. The NN training and test were performed in Matlab R2019b (Mathworks Inc., MA, USA). To train the NN, a Levenberg-Marquardt technique was used which converged to a desirable solution (residual norm-error $\leq 2\%$) after 162 epoches.

Fig. 4.4 compares the predicted force-displacement curves of the MREs with their experimental references. Table 4.1 summarizes the performance of the trained NN in predicting the force-displacement behavior of the MREs. Also, Fig. 4.5(a) shows the convergence of the NN training and Fig. 4.5(b) depicts the correlation between the NN-predicted force and experimental forces for the training dataset. The results showed a regression coefficient of 0.97, a goodness-of-fit of 0.97 and a mean-absolute-error (MAE) of 1.26 N across all the verification data.

In comparison with the literature, the trained NN showed superior accuracy compared to [80], [78], and [44]. One of the reasons for the superior performance of the proposed NN might be due to the inclusion of rate-dependency through adding $\dot{s}$ to the features vector.

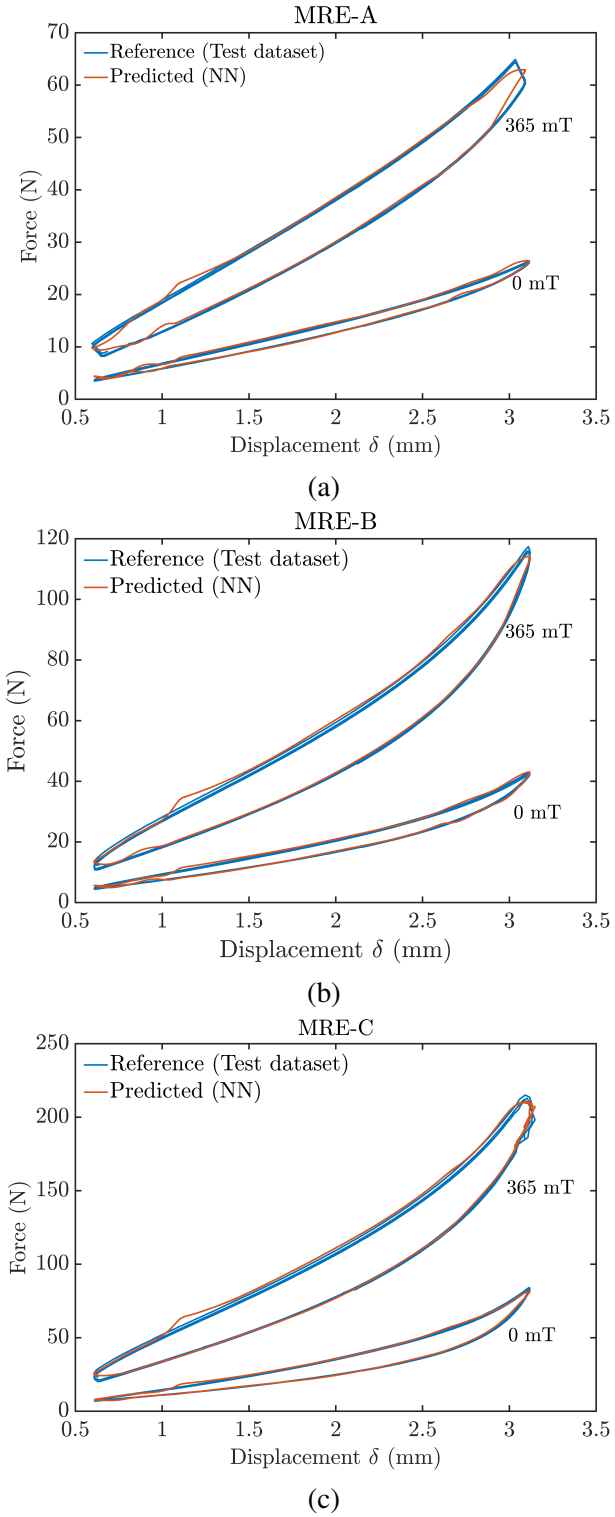

Figure 4.4: Comparison of the predicted force-displacement characteristics (a) MRE-A (b) MRE-B (middle) and (c) MRE-C versus their experimental reference.

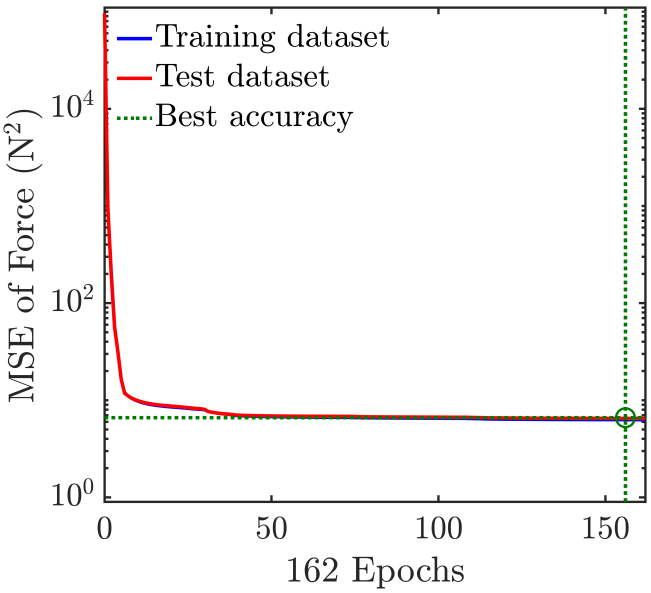

(a)

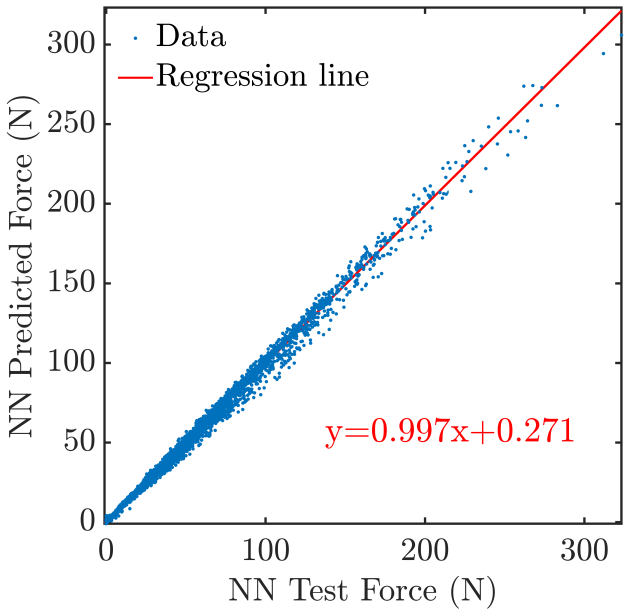

(b)

Figure 4.5: (a) convergence diagram of the training of the NN, (b) the regression between the forces in the test dataset and predicted forces resulted from NN.

4.2.6 Nearest Neighbor Search for finding the desired magnetic field

As discussed above, the parameter of interest in this study is the external magnetic field which is the only controllable parameter. Therefore, an iterative NNS approach with linear search method was implemented for finding the desired magnetic field given a specific tuple $\begin{pmatrix} s & \dot{s} & F & \zeta \end{pmatrix}$. The NNS was defined such that finds the best B which satisfies the minimization problem stated in Eq. 44. The implementation of NNS was performed in Matlab R2019b.

$$\forall \begin{pmatrix} s & \dot{s} & F & \zeta \end{pmatrix} \quad \exists B \quad \| \quad |F - \text{NN}(s, \dot{s}, B, \zeta)| \leq \varepsilon, \tag{44}$$

where ε was the radius of neighborhood set as $\varepsilon = 1.26$N for the NNS. The set ϵ matches the MAE of the NN for the test dataset.

4.3 Validation Study

In order to study the usability and validity of the trained NN and the implemented NNS experimental, the experimental data reported in [30] was used. The available experimental data was related to a pulse replication experiment. In [30], Hooshiar *et al.* controlled the external magnetic field on an MRE-based tactile display to generate similar forces to the human pulse forces on a dummy finger. In their experiment, a similar MRE to MRE-C of this study was used. The reference experiment had two parts. In the first part, the dummy finger would indent into MRE-C up to 4.5 mm at a constant rate of 1 $\frac{\text{mm}}{s}$ and afterward would keep its position.

The objective of this validation study was to find the external magnetic field required to replicate the forces as reported in [30]. To use the experimental data in the NNS, parameter c was set to 45 (for MRE-C). Also, the experimental s, $\dot{s}$, and F were used directly. The reference experimental dataset was composed of 4322 data samples. The controlled external magnetic field from the reference dataset was selected as the reference for comparison with the output of NNS. Fig. 4.6 shows the changes in force, magnetic field and displacement in MRE-C from the experiment used as input to the NNs. The reference dataset did not contain $\dot{s}$ information, therefore a two-point numerical differentiation was performed on δ data to obtain $\dot{s}$.

The average computation time to find the magnetic field was 4 ± 8 ms corresponding to a mini-

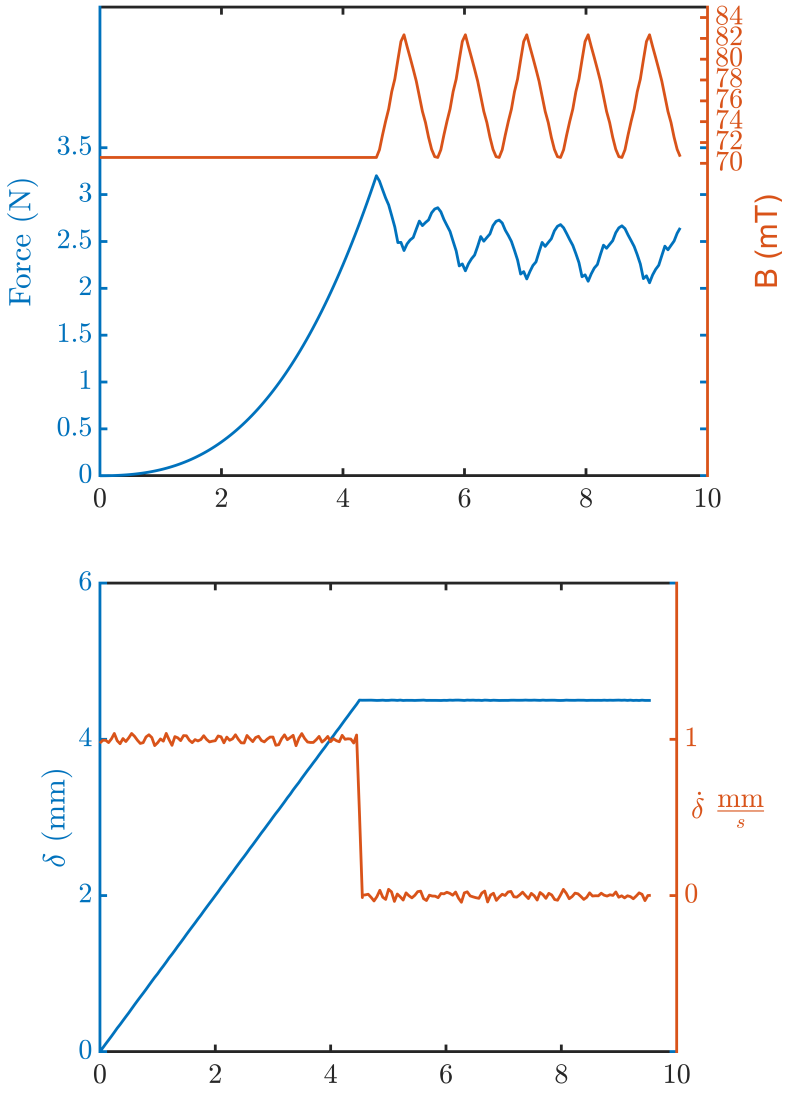

Figure 4.6: Input data from the reference experiment to NNS for finding the desired magnetic field to generate force as observed in the reference.

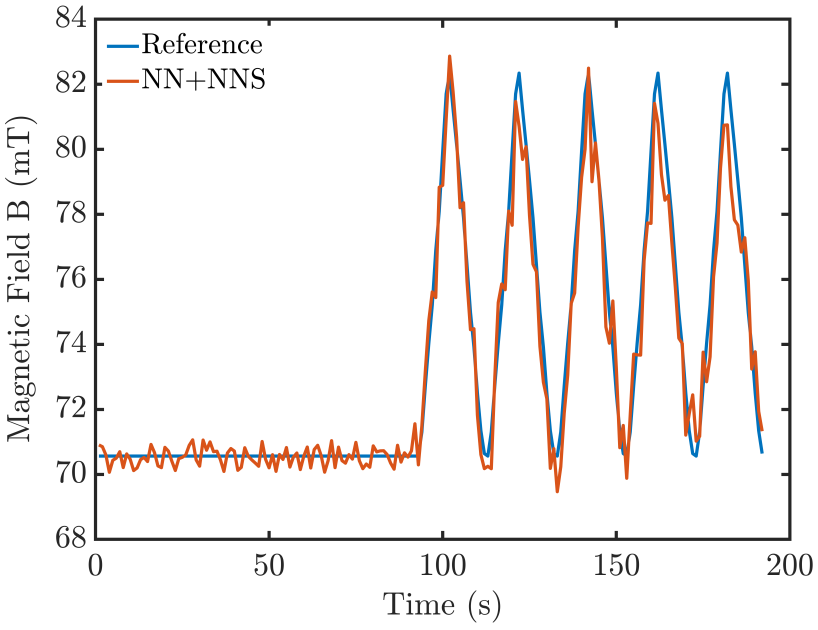

(a)

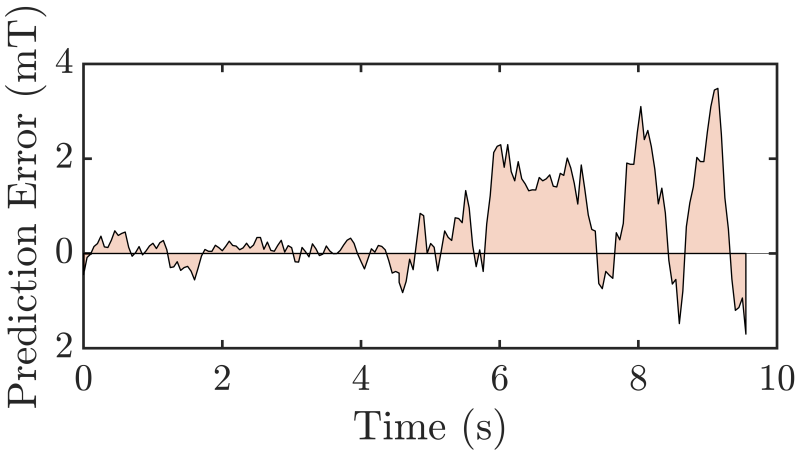

(b)

Figure 4.7: (a) Comparison of the reference magnetic field for radial pulse experiment witht the NN+NNS predicted magnetic fields, (b) temporal variation of the magnetic field prediction error obtained from NN+NNS.

mum refresh rate of approximately 83 Hz. Typically, passive force/torque feedback systems run at a refresh rate of less than 60 Hz, as the tactile receptors within human skin (Meissner Corpuscles) function around the same refresh rate. Fig. 4.7(a) shows the output of NNS linear search for finding the magnetic field. The NNS was able to predict the required magnetic force to reproduce the desired force. However, since the force data in the reference experiment had exhibited exponential relaxation (due to the viscoelastic nature of the MREs), ther error of prediction has increased with time. The reason is that the trained NN had failed to capture the force relaxation. In fact, force relaxation in MREs was not present in the training data, therefore, the NN has not captured it. Fig. 4.7(b) shows the prediction error between the reference magnetic fields and NN+NNS. the MAE of NN+NNS prediction was $1.14 \pm 1.48mT$ (3.2% of maximum magnetic field) and its maximum error was 3.64 mT (4.4% of the maximum magnetic field). The exhibited error showed that the NN+NNS has predicted the required magnetic field with less than 5% error.

4.4 Summary

In this study initially a control loop was proposed for controlling the frictional torque of MRE pads on the central shaft of the device. The control loop, necessitated utilization of a method to determine the required magnetic field to observe the desired force-displacement of the MRE. Since mechanistic models of the MREs are rigorous and complicated they are not suitable for control implementation. The main hypothesis of this study was that an accurate heuristic model of MRE, e.g., NN, can effectively capture the mechanical behavior of MREs. Such data-driven models if used in conjunction with a search method, e.g., NNS, can be used to find magnetic field required to observe a desired behavior in MREs. To test this hypothesis, two experimental validation tests were performed. First, an NN was trained with previously available experimental data and exhibited acceptable behavior in re-creating force-displacement curves of three classes of MREs. Afterward, an NNS method was used to find magnetic fields required to recreate a pulsatile force similar to [30]. The validation tests showed that the proposed NN, thanks to the inclusion of rate-dependency in the features vector, showed superior accuracy compare to representative studies of the literature. Also, it was inferred that combination of NN and NNS is a favorable option for the proposed control framework.

In future works, the proposed NN+NNS method could be incorporated in a torque control mechanism similar to TorMag and its force control performance could be investigated. Another expansion of this study could be utilization of recurrent NNs to account for the time-history (temporal effect) of force and displacement. The proposed NN fell short of capturing the force relaxation phenomenon observed in the reference validation test.

Chapter 5

Conclusion and Future Works

5.1 Conclusions

In Chapter 2, the effects of the shear modulus of polymer matrices and percentage of CIP on the force feedback range. Firstly, a variable magnetic permeability term was added to a recently-validated constitutive model. Also, twelve MREs with various CIP percentages and shear moduli were fabricated, characterized, and tested for their initial shear modulus and force feedback range in the proposed haptic feedback system. Comparison of the force ranges exhibited by different MREs with forces reported in the literature for various surgeries showed the versatility of the achievable forces that can be exploited for surgical applications on different biological tissues.

In Chapter 3, the structural optimization of the design of the MRE and TorMag device was performed. The aim of Chapter 2 was to address the limitation of the proposed magnetostriction-based force rendering in achieving near-zero forces in RCI applications. The results showed that the proposed method successfully found a feasible optimized design for TorMag and MRE. Also, since the proposed goal function was based on the system performance in the phase portrait, it could capture the system's dynamic response and eventually result in feasible dynamics for the system.

In Chapter 4, addressing another limitation of the proposed system was attempted. As shown analytically, the rise-time of the motor controller affects the coverage of the desired phase portrait. Thus, in Chapter 4, the feasibility of using a neural network-based method was suggested to control the desired magnet separation. The proposed neural network-based control system exhibited a faster response time in calculating the required magnet separation than the previously proposed nonlinear solver. Also, this control system showed a shorter rise-time in comparison to the previous study on

TorMag for rendering blood pressure pulse forces in a telerobotic RCI .

In this research, the stated research objectives in Sec. 1.3 were successfully obtained. More specifically, the prominent findings were that increasing the filler percentage from 10% to 40% increased the force feedback range up to 288%. Through structural optimization, the coverage of phase portrait increased to 100% in two representative experimental use-cases. Finally, the proposed neural network with nearest neighbour search control architecture increased the response time of the force rendering system, i.e. TorMag.

5.2 Future Studies

The present research can be further improved by:

(1) adopting a viscoelastic constitutive model that allows for accounting for temporal changes in rendered forces, especially for sustained forces over long periods,

(2) using other matrix and filler components such as Polydimethylsiloxane (PDMS) and cobalt nanoparticles that may exhibit similar magnetostriction with smaller volume fractions,

(3) exploiting the piezoresistivity of MREs to directly measure the contact force on the MREs in real-time,

(4) investigating other robotic surgery tasks such as minimally invasive laparoscopic and endoluminal tasks, especially on very soft tissues, e.g., brain and eye,

(5) adoption of other learning-based solvers for a controller such as support-vector regression and random forests, and

(6) utilization of recurrent neural networks to account for the time-history (temporal effect) in force as the proposed NN fell short of capturing the force relaxation phenomenon caused by viscoelasticity of the MREs,

(7) applying the obtained rise-time (t_r) based on NN+NNS to phase-portrait desciribed in chapter 3 for optimizing the performance of the system trough modifying the $\dot{F}_r$.

Bibliography

[1] George A. Mensah, Gregory A. Roth, and Valentin Fuster. The global burden of cardiovascular diseases and risk factors: 2020 and beyond. *Journal of the American College of Cardiology*, 74(20):2529–2532, 2019.

[2] WHO. Cardiovascular diseases (cvds) factsheets,, 2016.

[3] Dasdo A Sinaga, Alyssa S Sim, Hee Hwa Ho, Fahim Haider Jafary, Jason Loh, Yau Wei Ooi, Julian Tan, and Paul Ong. Tct-408 de novo small vessel coronary disease: To stent or not to stent? can drug coated balloon be a safe and effective alternative to modern drug eluting stent? *Journal of the American College of Cardiology*, 66(15 Supplement):B166, 2015.

[4] Masato Nakamura. Angiography is the gold standard and objective evidence of myocardial ischemia is mandatory if lesion severity is questionable. *Circulation Journal*, pages 1012101024–1012101024, 2011.

[5] Faisal Hasan and Johannes Bonatti. Robotically assisted percutaneous coronary intervention: benefits to the patient and the cardiologist. *Expert Review of Cardiovascular Therapy*, 13(11):1165–1168, 2015.

[6] RV Leena and NK Shyamkumar. Glove perforations during interventional radiological procedures. *Cardiovascular and interventional radiology*, 33(2):375–378, 2010.

[7] George Dangas, Ioannis Iakovou, Eugenia Nikolsky, Eve D Aymong, Gary S Mintz, Nicholas N Kipshidze, Alexandra J Lansky, Issam Moussa, Gregg W Stone, Jeffrey W Moses, et al. Contrast-induced nephropathy after percutaneous coronary interventions in relation to

chronic kidney disease and hemodynamic variables. *The American journal of cardiology*, 95(1):13–19, 2005.

[8] Ryan A. Beasley. Medical robots: Current systems and research directions. *Journal of Robotics*, 13(11):1165–1168, 2012. PMID: 26377605.

[9] A. Hooshiar, S. Najarian, and J. Dargahi. Haptic telerobotic cardiovascular intervention: A review of approaches, methods, and future perspectives. *IEEE Reviews in Biomedical Engineering*, 13:32–50, 2020.

[10] Prapa Kanagaratnam, Michael Koa-Wing, Daniel T Wallace, Alex S Goldenberg, Nicholas S Peters, and D Wyn Davies. Experience of robotic catheter ablation in humans using a novel remotely steerable catheter sheath. *Journal of Interventional Cardiac Electrophysiology*, 21(1):19–26, 2008.

[11] Chad M Dugas and Jeffrey M Schussler. Advanced technology in interventional cardiology: a roadmap for the future of precision coronary interventions. *Trends in cardiovascular medicine*, 26(5):466–473, 2016.

[12] Hedyeh Rafii-Tari, Celia V Riga, Christopher J Payne, Mohamad S Hamady, Nicholas JW Cheshire, Colin D Bicknell, and Guang-Zhong Yang. Reducing contact forces in the arch and supra-aortic vessels using the magellan robot. *Journal of Vascular Surgery*, 64(5):1422–1432, 2016.

[13] Tejas M Patel, Sanjay C Shah, and Samir B Pancholy. Long distance tele-robotic-assisted percutaneous coronary intervention: a report of first-in-human experience. *EClinicalMedicine*, 14:53–58, 2019.

[14] Carlos Tercero, Seiichi Ikeda, Tomomi Uchiyama, Toshio Fukuda, Fumihito Arai, Yuta Okada, Yoshinari Ono, Ryohei Hattori, Tokunori Yamamoto, Makoto Negoro, et al. Autonomous catheter insertion system using magnetic motion capture sensor for endovascular surgery. *The International Journal of Medical Robotics and Computer Assisted Surgery*, 3(1):52–58, 2007.

[15] Steve Ramcharitar, Mark S. Patterson, Robert Jan van Geuns, Carlos van Meighem, and Patrick W. Serruys. Technology insight: magnetic navigation in coronary interventions. *Nature Clinical Practice Cardiovascular Medicine*, 5(3):148–156, Mar 2008.

[16] Chad Dugas and Jeffrey Schussler. Advanced technology in interventional cardiology – a roadmap for the future of precision coronary interventions. *Trends in Cardiovascular Medicine*, 26, 02 2016.

[17] Nathaniel R Smilowitz, Jeffrey W Moses, Fernando A Sosa, Benjamin Lerman, Yasir Qureshi, Kate E Dalton, Lauren T Privitera, Diane Canone-Weber, Varinder Singh, Martin B Leon, et al. Robotic-enhanced pci compared to the traditional manual approach. *The Journal of invasive cardiology*, 26(7):318–321, 2014.

[18] Kamran Ahmed, Aoife N Keeling, Morkos Fakhry, Hutan Ashrafian, Rajesh Aggarwal, Peter A Naughton, Ara Darzi, Nicholas Cheshire, Thanos Athanasiou, and Mohammed Hamady. Role of virtual reality simulation in teaching and assessing technical skills in endovascular intervention. *Journal of Vascular and Interventional Radiology*, 21(1):55–66, 2010.

[19] Hedyeh Rafii-Tari, Christopher J Payne, and Guang-Zhong Yang. Current and emerging robot-assisted endovascular catheterization technologies: a review. *Annals of biomedical engineering*, 42(4):697–715, 2014.

[20] Hedyeh Rafii-Tari, Christopher J Payne, Colin Bicknell, Ka-Wai Kwok, Nicholas JW Cheshire, Celia Riga, and Guang-Zhong Yang. Objective assessment of endovascular navigation skills with force sensing. *Annals of biomedical engineering*, 45(5):1315–1327, 2017.

[21] Yu Song, Shuxiang Guo, Xuanchun Yin, Linshuai Zhang, Hideyuki Hirata, Hidenori Ishihara, and Takashi Tamiya. Performance evaluation of a robot-assisted catheter operating system with haptic feedback. *Biomedical microdevices*, 20(2):50, 2018.

[22] Klaus A Hausegger, Peter Schedlbauer, Hannes A Deutschmann, and Kurt Tiesenhausen. Complications in endoluminal repair of abdominal aortic aneurysms. *European journal of radiology*, 39(1):22–33, 2001.

[23] Shuxiang Guo, Mingyang Qin, Nan Xiao, Yuan Wang, Weili Peng, and Xianqiang Bao. High precise haptic device for the robotic catheter navigation system. In *2016 IEEE International Conference on Mechatronics and Automation*, pages 2524–2529. IEEE, 2016.

[24] Mark E Jacoby, Manivannan Veerasamy, and Ryan D Madder. Robotic percutaneous coronary intervention. In *Textbook of Catheter-Based Cardiovascular Interventions*, pages 133–143. Springer, 2018.

[25] Christopher J Payne, Hedyeh Rafii-Tari, and Guang-Zhong Yang. A force feedback system for endovascular catheterisation. In *2012 IEEE/RSJ International Conference on Intelligent Robots and Systems*, pages 1298–1304. IEEE, 2012.

[26] Yasuo Okumura, Susan B Johnson, T Jared Bunch, Benhur D Henz, Christine J O'brien, and Douglas L Packer. A systematical analysis of in vivo contact forces on virtual catheter tip/tissue surface contact during cardiac mapping and intervention. *Journal of cardiovascular electrophysiology*, 19(6):632–640, 2008.

[27] Luigi Di Biase, Andrea Natale, Conor Barrett, Carmela Tan, Claude S Elayi, Chi Keong Ching, Paul Wang, AMIN AL-AHMAD, Mauricio Arruda, J David Burkhardt, et al. Relationship between catheter forces, lesion characteristics,"popping," and char formation: experience with robotic navigation system. *Journal of cardiovascular electrophysiology*, 20(4):436–440, 2009.

[28] Stuart Schecter, Wei Lin, Aasha Gopal, Roger Fan, and Eric Rashba. Haptics and the heart: Force and tactile feedback system for cardiovascular interventions. *Cardiovascular Revascularization Medicine*, 19(6):36–40, 2018.

[29] K. K. Jain. Personalized management of cardiovascular disorders. *Medical Principles and Practice*, 26(5):399–414, 2017.

[30] Amir Hooshiar, Ali Alkhalaf, and Javad Dargahi. Development and assessment of a stiffness display system for minimally invasive surgery based on smart magneto-rheological elastomers. *Materials Science and Engineering: C*, 108:110409, 2020.

[31] Amir Hooshiar, Masoud Razban, Naghmeh M Bandari, and Javad Dargahi. Sensing principle for real-time characterization of viscoelasticity in the beating myocardial tissue. In *2017 IEEE International Conference on Computational Intelligence and Virtual Environments for Measurement Systems and Applications (CIVEMSA)*, pages 72–77. IEEE, 2017.

[32] N. Bandari, J. Dargahi, and M. Packirisamy. Miniaturized optical force sensor for minimally invasive surgery with learning-based nonlinear calibration. *IEEE Sensors Journal*, pages 1–1, 2019.

[33] Naghmeh M Bandari, Amir Hooshair, Muthukumaran Packirisamy, and Javad Dargahi. Optical fiber array sensor for lateral and circumferential force measurement suitable for minimally invasive surgery: Design, modeling and analysis. In *Specialty Optical Fibers*, pages JTu4A–44. Optical Society of America, 2016.

[34] Amir Hooshiar, Naghmeh M Bandari, and Javad Dargahi. Image-based estimation of contact forces on catheters for robot-assisted cardiovascular intervention. In *Proc. Hamlyn Symp. Med. Robot.*, pages 119–120, 2018.

[35] Pegah Yaftian, Naghmeh Bandari, Amir Hooshiar, and Javad Dargahi. Image-based contact detection and static force estimation on steerable rfa catheters. In *2020 International Conference on Biomedical Innovations and Applications (BIA)*, pages 57–60. IEEE, 2020.

[36] Mohammad Jolaei, Amir Hooshiar, Javad Dargahi, and Muthukumaran Packirisamy. Toward task autonomy in robotic cardiac ablation: Learning-based kinematic control of soft tendon-driven catheters. *Soft Robotics*, 2020.

[37] Amir Hooshiar, Amir Sayadi, Javad Dargahi, and Siamak Najarian. Integral-free spatial orientation estimation method and wearable rotation measurement device for robot-assisted catheter intervention. *IEEE/ASME Transactions on Mechatronics*, 2021.

[38] Jong Seok Oh, Young Min Han, and Seung Bok Choi. Design and performance evaluation of mr tactile device for medical application. In *Applied Mechanics and Materials*, volume 433, pages 869–872. Trans Tech Publ, 2013.

[39] Jong-Seok Oh, Jin-Kyu Kim, and Seung-Bok Choi. Experimental test of mr fluid based tactile device for minimally invasive surgery. In *Active and Passive Smart Structures and Integrated Systems 2013*, volume 8688, page 86882C. International Society for Optics and Photonics, 2013.

[40] Alex Mazursky, Jeong-Hoi Koo, and Tae-Heon Yang. Design, modeling, and evaluation of a slim haptic actuator based on electrorheological fluid. *Journal of Intelligent Material Systems and Structures*, page 1045389X19836172, 2019.

[41] Amy Kyungwon Han, Jung Hwa Bae, Katerina C Gregoriou, Christopher J Ploch, Roger E Goldman, Gary H Glover, Bruce L Daniel, and Mark R Cutkosky. Mr-compatible haptic display of membrane puncture in robot-assisted needle procedures. *IEEE transactions on haptics*, 11(3):443–454, 2018.

[42] Hiroshi Yanatori, Kazuki Tsuji, Konomu Abe, Kenji Iwasaki, and Takashi Mineta. Fabrication and characterization of an arrayed shape memory alloy thick film actuator device for planar tactile displays. *IEEJ Transactions on Sensors and Micromachines*, 139(1):15–20, 2019.

[43] Amir Hooshiar, Alireza Payami, Javad Dargahi, and Siamak Najarian. Magnetostriction-based force feedback for robot-assisted cardiovascular surgery using smart magnetorheological elastomers. *Mechanical Systems and Signal Processing*, 161:107918, 2021.

[44] Ashkan Dargahi, Subhash Rakheja, and Ramin Sedaghati. Development of a field dependent prandtl-ishlinskii model for magnetorheological elastomers. *Materials & Design*, 166:107608, 2019.

[45] Mostafa Asadi Khanouki, Ramin Sedaghati, and Masoud Hemmatian. Experimental characterization and microscale modeling of isotropic and anisotropic magnetorheological elastomers. *Composites Part B: Engineering*, 176:107311, 2019.

[46] Alireza Payami, Amir Hooshiar, Ali Alkhalaf, and Javad Dargahi. Modeling of rate-dependent force-displacement behavior of mres using neural networks for torque feedback applications. In *2020 8th International Conference on Control, Mechatronics and Automation (ICCMA)*, pages 58–62. IEEE, 2020.

[47] Smita Kanjanapas, Cara M Nunez, Sophia R Williams, Allison M Okamura, and Ming Luo. Design and analysis of pneumatic 2-dof soft haptic devices for shear display. *IEEE Robotics and Automation Letters*, 4(2):1365–1371, 2019.

[48] Martin Culjat, Chih-Hung King, Miguel Franco, James Bisley, Warren Grundfest, and Erik Dutson. Pneumatic balloon actuators for tactile feedback in robotic surgery. *Industrial Robot: An International Journal*, 35(5):449–455, 2008.

[49] Pyunghwa Kim, Soomin Kim, Young-Dai Park, and Seung-Bok Choi. Force modeling for incisions into various tissues with mrf haptic master. *Smart Materials and Structures*, 25(3):035008, 2016.

[50] Okan Topcu, Yiğit Taşcıoğlu, and Erhan Ilhan Konukseven. Design and multi-physics optimization of rotary mrf brakes. *Results in physics*, 8:805–818, 2018.

[51] Nicola Sgambelluri, Enzo P Scilingo, Rocco Rizzo, and Antonio Bicchi. A free-hand haptic interface based on magnetorheological fluids. In *The Sense of Touch and its Rendering*, pages 155–178. Springer, 2008.

[52] Alireza Payami, Javad Dargahi, and Amir Hooshiar. Performance analysis of magnetorheological elastomer composites for telerobotic force feedback rendering. *Advanced Composites and Hybrid Materials (under-review)*, 2021.

[53] Alireza Payami, Javad Dargahi, and Amir Hooshiar. Structural optimization of a magnetostriction-based force feedback system for telerobotic intervention. In *2021 IEEE International Symposium on Robotic and Sensors Environments (ROSE) (ROSE 2021)*, pages 1–7. IEEE, 2021.

[54] Yanliang Qiao, Jiangtao Zhang, Mei Zhang, Lisheng Liu, and Pengcheng Zhai. A magnetic field-and frequency-dependent dynamic shear modulus model for isotropic silicone rubber-based magnetorheological elastomers. *Composites Science and Technology*, 204:108637, 2021.

[55] Yunpeng Wang, Li Ding, Chunyu Zhao, Sheng Wang, Shouhu Xuan, Han Jiang, and Xinglong Gong. A novel magnetorheological shear-stiffening elastomer with self-healing ability. *Composites Science and Technology*, 168:303–311, 2018.

[56] Lin Ge, Xinglong Gong, Yu Wang, and Shouhu Xuan. The conductive three dimensional topological structure enhanced magnetorheological elastomer towards a strain sensor. *Composites Science and Technology*, 135:92–99, 2016.

[57] Ali Alkhalaf, Amir Hooshiar, and Javad Dargahi. Composite magnetorheological elastomers for tactile displays: Enhanced mr-effect through bi-layer composition. *Composites Part B: Engineering*, 190:107888, 2020.

[58] Ali Alkhalaf, Amir Hooshiar, and Javad Dargahi. Enhancement of mr-effect in magnetorheological elastomers through bi-layer composition: Theory and validation. In *Proceeding of 30th International Conference on Adaptive Structures and Technologies*, volume 1, pages 1–2. Concordia University, 2019.

[59] Zhengyang Chen, Shuxiang Guo, and Wei Zhou. A novel clamping mechanism for circumferential force feedback device of the vascular interventional surgical robot. In *2020 IEEE International Conference on Mechatronics and Automation (ICMA)*, pages 1625–1630. IEEE, 2020.

[60] Ashkan Dargahi, Ramin Sedaghati, and Subhash Rakheja. On the properties of magnetorheological elastomers in shear mode: Design, fabrication and characterization. *Composites Part B: Engineering*, 159:269–283, 2019.

[61] Rubber, vulcanized or thermoplastic – determination of compression stress-strain properties. Standard, International Organization for Standardization, Geneva, CH, 10 2017.

[62] Anil K Bastola and Mokarram Hossain. A review on magneto-mechanical characterizations of magnetorheological elastomers. *Composites Part B: Engineering*, page 108348, 2020.

[63] Dirk W Schubert, Siegfried Werner, Ingo Hahn, and Veronika Solovieva. Effect of particle size

and size distribution on the permeability of soft magnetic liquid silicone rubber composites. *Composites Science and Technology*, 177:26–33, 2019.

[64] Xavier Oliver and C Agelet de Saracibar. Continuum mechanics for engineers. *Theory and problems*, 2017.

[65] Luis Dorfmann and Ray W Ogden. *Nonlinear theory of electroelastic and magnetoelastic interactions*, volume 1. Springer, 2014.

[66] A Dorfmann and RW Ogden. Some problems in nonlinear magnetoelasticity. *Zeitschrift für angewandte Mathematik und Physik ZAMP*, 56(4):718–745, 2005.

[67] Anil K Bastola, Milan Paudel, and Lin Li. Magnetic circuit analysis to obtain the magnetic permeability of magnetorheological elastomers. *Journal of Intelligent Material Systems and Structures*, 29(14):2946–2953, 2018.

[68] Stephan Rudykh and Katia Bertoldi. Stability of anisotropic magnetorheological elastomers in finite deformations: a micromechanical approach. *Journal of the Mechanics and Physics of Solids*, 61(4):949–967, 2013.

[69] A Bagheri, D Taghizadeh, and H Darijani. On the behavior of rotating thick-walled cylinders made of hyperelastic materials. *Meccanica*, 51(3):673–692, 2016.

[70] Takehito Kikuchi, Yusuke Kobayashi, Mika Kawai, and Tetsu Mitsumata. Elastic properties of magnetorheological elastomers in a heterogeneous uniaxial magnetic field. *International journal of molecular sciences*, 19(10):3045, 2018.

[71] Yogesh Thakur, Jeffrey S Bax, David W Holdsworth, and Maria Drangova. Design and performance evaluation of a remote catheter navigation system. *IEEE Transactions on biomedical engineering*, 56(7):1901–1908, 2009.

[72] Haoyang Yu, Hongbo Wang, Jingyuan Chang, Jianye Niu, Fuhao Wang, Yonggan Yan, Hesuo Tian, Junyu Fang, and Haixia Lu. A novel vascular intervention surgical robot based on force feedback and flexible clamping. *Applied Sciences*, 11(2):611, 2021.

[73] Hamed Azarnoush, Samaneh Siar, Robin Sawaya, Gmaan Al Zhrani, Alexander Winkler-Schwartz, Fahad Eid Alotaibi, Abdulgadir Bugdadi, Khalid Bajunaid, Ibrahim Marwa, Abdulrahman Jafar Sabbagh, et al. The force pyramid: a spatial analysis of force application during virtual reality brain tumor resection. *Journal of neurosurgery*, 127(1):171–181, 2016.

[74] Fumitaro Masaki, Franklin King, Takahisa Kato, Hisashi Tsukada, Yolonda Lorig Colson, and Nobuhiko Hata. Technical validation of multi-section robotic bronchoscope with first person view control for transbronchial biopsies of peripheral lung. *IEEE Transactions on Biomedical Engineering*, 2021.

[75] Siyang Zuo, Zhen Wang, Tianci Zhang, and Baojun Chen. A novel master–slave intraocular surgical robot with force feedback. *The International Journal of Medical Robotics and Computer Assisted Surgery*, page e2267, 2021.

[76] Christopher R Wottawa, Bradley Genovese, Bryan N Nowroozi, Steven D Hart, James W Bisley, Warren S Grundfest, and Erik P Dutson. Evaluating tactile feedback in robotic surgery for potential clinical application using an animal model. *Surgical endoscopy*, 30(8):3198–3209, 2016.

[77] Min Sang, Sheng Wang, Mei Liu, Linfeng Bai, Wanquan Jiang, Shouhu Xuan, and Xinglong Gong. Fabrication of a piezoelectric polyvinylidene fluoride/carbonyl iron (pvdf/ci) magnetic composite film towards the magnetic field and deformation bi-sensor. *Composites Science and Technology*, 165:31–38, 2018.

[78] Yang Yu, Yancheng Li, and Jianchun Li. Nonparametric modeling of magnetorheological elastomer base isolator based on artificial neural network optimized by ant colony algorithm. *Journal of Intelligent Material Systems and Structures*, 26(14):1789–1798, 2015.

[79] Dingxin Leng, Kai Xu, Yong Ma, Guijie Liu, and Lingyu Sun. Modeling the behaviors of magnetorheological elastomer isolator in shear-compression mixed mode utilizing artificial neural network optimized by fuzzy algorithm (annofa). *Smart Materials and Structures*, 27(11):115026, 2018.

[80] H. Vatandoost, S. M. Sajjadi Alehashem, M. Norouzi, H. Taghavifar, and Y. Ni. A supervised artificial neural network-assisted modeling of magnetorheological elastomers in tension–compression mode. *IEEE Transactions on Magnetics*, 55(12):1–8, Dec 2019.

Appendix A

Matlab Code for Phase-portrait Estimation

```
clc;
clear;
close all;

Ri = 0.004; %m
Ro = 0.011; %m
mu_d = 0.2; %mu_d
t = 0.02; %mm
bz=0;
w2=20; %roller radius=20mm
sdot=0.12; %rise time
mu0 = 4*3.1415*1e-7;
lambda1=zeros(3,4);
Torques=zeros(3,4);
G0_array=[100000 200000 300000]; %Pa
mu_r_array=[2 2.2 3.8 6];

for i=1:3
    for j=1:4
        s=45e-3;
        a = 0.440000*(s*1000).^-1.3/6*mu_r_array(j);
        Gamma1 = (mu0*mu_r_array(j))^(-1)*(a^2/(Ri*Ro) - Ro*bz^2/Ri) -
t*a^2*(mu_r_array(j) - 1)/(2*mu0*mu_r_array(j))*(1/Ri^2 - 1/(Ri*Ro));
        Gamma2 = -(mu0*mu_r_array(j))^(-1)*(a^2/Ri^2 - bz^2)-t*a^2*(mu_r_array(j) -
1)/(mu0*mu_r_array(j))*(1/Ri^2 - 1/(Ri*Ro));
        l1 = (8*G0_array(i) - Gamma1 -
sqrt(16*G0_array(i)^2-8*G0_array(i)*Gamma2-16*G0_array(i)*Gamma1+Gamma1^2))/(4*G0_a
rray(i));
        L=4*(l1 - 1) - 2*(l1 - 1)^2;
        T11 = G0_array(i)*L - (mu0*mu_r_array(j))^(-1)*(a^2/Ri^2 - bz^2);
        zeta=(2*3.14*t*Ri^2*mu_d)/l1;
        Tr=-zeta*T11/l1;
        Torques45(i,j)=Tr*1000; %1000 is to convert Nm to mNm
        F45(i,j)=Torques45(i,j)/w2;
        lambda1(i,j)=l1;

    end
end

for i=1:3
    for j=1:4
        s=46e-3;
        a = 0.440000*(s*1000).^-1.3/6*mu_r_array(j);
        Gamma1 = (mu0*mu_r_array(j))^(-1)*(a^2/(Ri*Ro) - Ro*bz^2/Ri) -
t*a^2*(mu_r_array(j) - 1)/(2*mu0*mu_r_array(j))*(1/Ri^2 - 1/(Ri*Ro));
        Gamma2 = -(mu0*mu_r_array(j))^(-1)*(a^2/Ri^2 - bz^2)-t*a^2*(mu_r_array(j) -
1)/(mu0*mu_r_array(j))*(1/Ri^2 - 1/(Ri*Ro));
        l1 = (8*G0_array(i) - Gamma1 -
sqrt(16*G0_array(i)^2-8*G0_array(i)*Gamma2-16*G0_array(i)*Gamma1+Gamma1^2))/(4*G0_a
rray(i));
```

```
        L=4*(l1 - 1) - 2*(l1 - 1)^2;
        T11 = G0_array(i)*L - (mu0*mu_r_array(j))^(-1)*(a^2/Ri^2 - bz^2);
        zeta=(2*3.14*t*Ri^2*mu_d)/l1;
        Tr=-zeta*T11/l1;
        Torques46(i,j)=Tr*1000; %1000 is to convert Nm to mNm
        lambda1(i,j)=l1;

    end
end

ds=1;
dTrds45=(Torques45-Torques46)/ds;
dFds45=(1/w2)*dTrds45;
Fdot45=dFds45*sdot;

for i=1:3
    for j=1:4
        s=95e-3;
        a = 0.440000*(s*1000).^-1.3/6*mu_r_array(j);
        Gamma1 = (mu0*mu_r_array(j))^(-1)*(a^2/(Ri*Ro) - Ro*bz^2/Ri) -
t*a^2*(mu_r_array(j) - 1)/(2*mu0*mu_r_array(j))*(1/Ri^2 - 1/(Ri*Ro));
        Gamma2 = -(mu0*mu_r_array(j))^(-1)*(a^2/Ri^2 - bz^2)-t*a^2*(mu_r_array(j) -
1)/(mu0*mu_r_array(j))*(1/Ri^2 - 1/(Ri*Ro));
        l1 = (8*G0_array(i) - Gamma1 -
sqrt(16*G0_array(i)^2-8*G0_array(i)*Gamma2-16*G0_array(i)*Gamma1+Gamma1^2))/(4*G0_a
rray(i));
        L=4*(l1 - 1) - 2*(l1 - 1)^2;
        T11 = G0_array(i)*L - (mu0*mu_r_array(j))^(-1)*(a^2/Ri^2 - bz^2);
        zeta=(2*3.14*t*Ri^2*mu_d)/l1;
        Tr=-zeta*T11/l1;
        Torques95(i,j)=Tr*1000; %1000 is to convert Nm to mNm
        F95(i,j)=Torques95(i,j)/w2;
        lambda1(i,j)=l1;

    end
end

for i=1:3
    for j=1:4
        s=94e-3;
        a = 0.440000*(s*1000).^-1.3/6*mu_r_array(j);
        Gamma1 = (mu0*mu_r_array(j))^(-1)*(a^2/(Ri*Ro) - Ro*bz^2/Ri) -
t*a^2*(mu_r_array(j) - 1)/(2*mu0*mu_r_array(j))*(1/Ri^2 - 1/(Ri*Ro));
        Gamma2 = -(mu0*mu_r_array(j))^(-1)*(a^2/Ri^2 - bz^2)-t*a^2*(mu_r_array(j) -
1)/(mu0*mu_r_array(j))*(1/Ri^2 - 1/(Ri*Ro));
        l1 = (8*G0_array(i) - Gamma1 -
sqrt(16*G0_array(i)^2-8*G0_array(i)*Gamma2-16*G0_array(i)*Gamma1+Gamma1^2))/(4*G0_a
rray(i));
        L=4*(l1 - 1) - 2*(l1 - 1)^2;
        T11 = G0_array(i)*L - (mu0*mu_r_array(j))^(-1)*(a^2/Ri^2 - bz^2);
```

```
        zeta=(2*3.14*t*Ri^2*mu_d)/l1;
        Tr=-zeta*T11/l1;
        Torques94(i,j)=Tr*1000; %1000 is to convert Nm to mNm
        lambda1(i,j)=l1;

    end
end

ds=1;
dTrds95=(Torques94-Torques95)/ds;
dFds95=(1/w2)*dTrds95;
Fdot95=dFds95*sdot;

f=1;


for h=1:3
    for k=1:4

x1=[F45(h,k) F95(h,k) F95(h,k) F45(h,k) F45(h,k)] ;
y1=[Fdot45(h,k) Fdot95(h,k) -Fdot95(h,k) -Fdot45(h,k) Fdot45(h,k)];
subplot(3,4,f)
hold on;
plot(x1,y1);
f=f+1;
    end

end
```

Appendix B

Matlab Code for Structural Optimization

```
%%%%%%%%%%%%%%%%%%%%%%%% Step 1: Define the goal function

function normd = Trapfunc2(x) %all in mm
clf
%% Initialization
Rii=x(1);
Roo=x(2);
tt=x(3);
SSmax=x(4);
smin=45e-3;
%% Unit conversion
Ri=Rii/1000 %m
Ro=Roo/1000%m
t=tt/1000%m
Smax=SSmax/1000%m

%% Constants
mu_d = 0.2; %mu_d
bz=0;
w2=0.020; %roller radius=20mm
sdot=1/0.12; %rise time
mu0 = 4*3.1415*1e-7;
lambda1=0;
Torques=0;
G0_array=300000 ; %Pa
mu_r_array=3.8;
%%

        s=smin;
        a = 0.440000*(s*1000).^-1.3/6*mu_r_array;
        Gamma1 = (mu0*mu_r_array)^(-1)*(a^2/(Ri*Ro) - Ro*bz^2/Ri) -
t*a^2*(mu_r_array - 1)/(2*mu0*mu_r_array)*(1/Ri^2 - 1/(Ri*Ro));
        Gamma2 = -(mu0*mu_r_array)^(-1)*(a^2/Ri^2 - bz^2)-t*a^2*(mu_r_array -
1)/(mu0*mu_r_array)*(1/Ri^2 - 1/(Ri*Ro));
        l1 = (8*G0_array - Gamma1 -
sqrt(16*G0_array^2-8*G0_array*Gamma2-16*G0_array*Gamma1+Gamma1^2))/(4*G0_array);
        L=4*(l1 - 1) - 2*(l1 - 1)^2;
        T11 = G0_array*L - (mu0*mu_r_array)^(-1)*(a^2/Ri^2 - bz^2);
        zeta=(2*3.14*t*Ri^2*mu_d)/l1;
        Tr=-zeta*T11/l1;
        Torques45=Tr; %1000 is to convert Nm to mNm
        F45=Torques45/w2;
%%
        s=smin+0.001;
        a = 0.440000*(s*1000).^-1.3/6*mu_r_array;
        Gamma1 = (mu0*mu_r_array)^(-1)*(a^2/(Ri*Ro) - Ro*bz^2/Ri) -
t*a^2*(mu_r_array - 1)/(2*mu0*mu_r_array)*(1/Ri^2 - 1/(Ri*Ro));
        Gamma2 = -(mu0*mu_r_array)^(-1)*(a^2/Ri^2 - bz^2)-t*a^2*(mu_r_array -
1)/(mu0*mu_r_array)*(1/Ri^2 - 1/(Ri*Ro));
        l1 = (8*G0_array - Gamma1 -
```

```
sqrt(16*G0_array^2-8*G0_array*Gamma2-16*G0_array*Gamma1+Gamma1^2))/(4*G0_array);
        L=4*(l1 - 1) - 2*(l1 - 1)^2;
        T11 = G0_array*L - (mu0*mu_r_array)^(-1)*(a^2/Ri^2 - bz^2);
        zeta=(2*3.14*t*Ri^2*mu_d)/l1;
        Tr=-zeta*T11/l1;
        Torques46=Tr; %1000 is to convert Nm to mNm
%%
ds=1;
dTrds45=(Torques45-Torques46)/ds;
dFds45=(1/w2)*dTrds45;
Fdot45=dFds45*sdot;
%%
        s=Smax;
        a = 0.440000*(s*1000).^-1.3/6*mu_r_array;
        Gamma1 = (mu0*mu_r_array)^(-1)*(a^2/(Ri*Ro) - Ro*bz^2/Ri) -
t*a^2*(mu_r_array - 1)/(2*mu0*mu_r_array)*(1/Ri^2 - 1/(Ri*Ro));
        Gamma2 = -(mu0*mu_r_array)^(-1)*(a^2/Ri^2 - bz^2)-t*a^2*(mu_r_array -
1)/(mu0*mu_r_array)*(1/Ri^2 - 1/(Ri*Ro));
        l1 = (8*G0_array - Gamma1 -
sqrt(16*G0_array^2-8*G0_array*Gamma2-16*G0_array*Gamma1+Gamma1^2))/(4*G0_array);
        L=4*(l1 - 1) - 2*(l1 - 1)^2;
        T11 = G0_array*L - (mu0*mu_r_array)^(-1)*(a^2/Ri^2 - bz^2);
        zeta=(2*3.14*t*Ri^2*mu_d)/l1;
        Tr=-zeta*T11/l1;
        Torques95=Tr; %1000 is to convert Nm to mNm
        F95=Torques95/w2;
%%
        s=Smax-0.001;
        a = 0.440000*(s*1000).^-1.3/6*mu_r_array;
        Gamma1 = (mu0*mu_r_array)^(-1)*(a^2/(Ri*Ro) - Ro*bz^2/Ri) -
t*a^2*(mu_r_array - 1)/(2*mu0*mu_r_array)*(1/Ri^2 - 1/(Ri*Ro));
        Gamma2 = -(mu0*mu_r_array)^(-1)*(a^2/Ri^2 - bz^2)-t*a^2*(mu_r_array -
1)/(mu0*mu_r_array)*(1/Ri^2 - 1/(Ri*Ro));
        l1 = (8*G0_array - Gamma1 -
sqrt(16*G0_array^2-8*G0_array*Gamma2-16*G0_array*Gamma1+Gamma1^2))/(4*G0_array);
        L=4*(l1 - 1) - 2*(l1 - 1)^2;
        T11 = G0_array*L - (mu0*mu_r_array)^(-1)*(a^2/Ri^2 - bz^2);
        zeta=(2*3.14*t*Ri^2*mu_d)/l1;
        Tr=-zeta*T11/l1;
        Torques94=Tr; %1000 is to convert Nm to mNm
%%
ds=1;
dTrds95=(Torques94-Torques95)/ds;
dFds95=(1/w2)*dTrds95;
Fdot95=dFds95*sdot;
%%

x1=[F45 F95 F95 F45 F45] ;
y1=[Fdot45 Fdot95 -Fdot95 -Fdot45 Fdot45];
hold on;
```

```
plot(x1,y1);
%%
plux=0.5;
pldx=plux;
pluy=0.25;
pldy=-pluy;
prux=3;
prdx=prux;
pruy=1;%N/s
prdy=-pruy;
%%
dru=(F45-prux)^2+0*(Fdot45-pruy)^2;
%drd=(F45-prux)^2+(-Fdot45-pruy)^2;
dlu=(F95-plux)^2+(Fdot95-pluy)^2;
%dld=(F95-plux)^2+(-Fdot95-pluy)^2;

normd=dru+ dlu

x2=[pldx plux prux prdx pldx] ;
y2=[pldy pluy pruy prdy pldy];

hold on;
plot(x2,y2);

pause(0.1);

end % end of function

%%%%%%%%%%%%%%%%%%%%%%%% End of Step 1



%%%%%%%%%%%%%%%%%%%%%%%% Step 2: Calling the function

function [x,fval,exitflag,output,lambda,grad,hessian] = OptimTorque(x0)
%% This is an auto generated MATLAB file from Optimization Tool.
lb=[4  8 10 50];
ub=[4 15 50  200]
%% Start with the default options
options = optimoptions('fmincon');
%% Modify options setting
options = optimoptions(options,'Display', 'off');
[x,fval,exitflag,output,lambda,grad,hessian] = ...
fmincon(@Trapfunc2,x0,[],[],[],[],lb,ub,[],options);

%%%%%%%%%%%%%%%%%%%%%%%% End of Step 2
```